Thermal Impedance Match in Thermoelectric Generator Design for Maximum Net Power

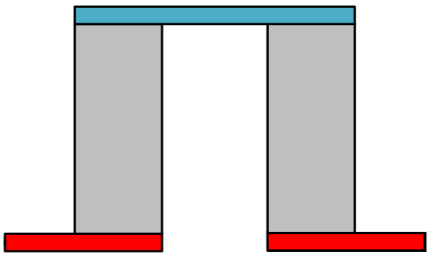

Master thesis

Diego Fraguas
Gísli Làrusson

Aalborg University
Department of Energy Technology
Pontoppidanstræde 101
DK-9220 Aalborg
http://es.aau.dk

AALBORG UNIVERSITY

STUDENT REPORT

Aalborg University
Department of Energy Technology
Pontoppidanstræde 101
DK-9220 Aalborg
http://es.aau.dk

Title:
Thermal Impedance Match in Thermoelectric Generator Design for Maximum Net Power

June 3, 2015

Theme:

Project Period:
Autumn Semester 2015

Project Group:
TEPE4-1001

Participant(s):
Diego Fraguas
Gísli Lárusson

Supervisor(s):
Alireza Rezaniakolaei
Thomas Condra

Copies: 3

Page Numbers: ??

Date of Completion:

Abstract:

In this project a TEG based WHRS is optimized for auto-mobile applications. To optimize the WHRS, the thermal impedance of the TEG has to be matched with the thermal impedance of the heat exchanger used to transfer the heat from the car engine exhaust gas to the TEG and the thermal impedance of the heat sink of the system.
The optimization procedure was based on an analytical model. The analytical model was tried to be validated by a CFD model and experimental work.
The thermal resistance prediction of the analytical model was found to be valid, however the TEG module performance was not.
The obtained optimal design was simulated in order to determine the feasibility of the WHRS.

Summary

The efficiency of a thermoelectric generator is influenced by the material properties and the temperature gradient across it. A TEG works as a thermal engine, it operates between a heat source and a heat sink and converts part of the heat into electrical power. The power production of a TEG module is maximized when its thermal impedance is matched with the thermal impedances of the heat exchangers used to transfer the heat from the source to the sink.

In this project, a TEG based waste heat recovery system for auto-mobile applications is optimized to maximize its net power production. Both air and water cooled WHRS are considered. An optimization problem based on an analytical model is set to achieve it.

This model was tried to be validated by experimental work. A experimental setup, described in this report, was designed. Three experiments were carried out at Aalborg University thermoelectrics laboratory.

In addition, a CFD simulation was developed in order to compare its results with the analytical model. However it was not achieved.

Finally, the performance of the optimized WHRS was predicted by the analytical model under different working conditions.

The results were not conclusive but an insight in the challenges within the WHRS design was obtained and the implementation of such a WHRS was determined feasible.

Preface

This report was written by Diego Fraguas and Gisli Larusson, group TEPE4-1001, during the 10^{th} semester of the program Thermal Energy and Process Engineering at Department of Energy Technology, Aalborg University. The project period spread from 2^{nd} of February until 3^{rd} of June. The report was written in Latex and the simulations were carried out with the softwares MATLAB and FLUENT. Furthermore the EES thermodynamic properties database was used. The applied citation style follows the Chicago style according to (author, year). The MATLAB scripts and FLUENT case files can be found on the attached CD ROM. In addition, the technical drawings of the experimental setup components can be found.

Aalborg University, June 3, 2015

Diego Fraguas Tejero
<dfragu13@student.aau.dk>

Gisli Larusson
<glarus1313@student.aau.dk>

Contents

Preface **vii**

1 Introduction **1**
1.1 Thermoelectric materials and their properties 2
1.2 Problem definition 5
1.3 Methodology 7

2 Analytical model **9**
2.1 TEG module electric model 9
2.2 WHRS thermal model 12
2.2.1 TEG module thermal model 13
2.2.2 Hot side heat exchanger model 14
2.2.3 Heat sink model 17

3 Experimental validation **23**
3.1 Experimental setup description 23
3.1.1 Hot side heat exchanger design 23
3.1.2 TEG-HS arrangement 25
3.2 Instrumentation 28
3.3 Experimental setup assembly 30
3.4 Experimental procedure 33
3.5 Experimental data and model comparison 34

4 Computational fluid dynamics **41**
4.1 Pre-Process 42
4.1.1 Solid modelling 42
4.1.2 Mesh generation 42
4.2 Process 44
4.2.1 CFD governing Equations 44
4.2.2 Physical models 45
4.3 Simulation boundary conditions 46
4.3.1 Thermodynamic properties 47
4.3.2 Simulations boundary conditions 47

4.3.3 Mesh independence study 53
4.3.4 FLUENT convergence criteria 56
4.4 Result and discussion 56

5 Optimization **59**
5.1 Problem definition 59
5.2 Optimization boundary conditions 61
5.3 Optimization tools 63
5.4 Optimization procedure 64
5.5 WHRS optimal designs 67

6 Analytical model results and discussion **69**
6.1 Water cooled WHRS results 69
6.1.1 Simulation 1. Performance for variable exhaust gas mass flow . 69
6.1.2 Simulation 2. Performance for variable electric load 71
6.1.3 Simulation 3. Performance for variable cooling water velocity . 74
6.2 Air cooled WHRS results 74
6.2.1 Simulation 1. Performance for variable exhaust gas mass flow . 75
6.2.2 Simulation 2. Performance for variable electric load 76
6.2.3 Simulation 3. Performance for variable cooling air velocity . . . 77

7 Conclusion **79**
7.1 Future work 80

Bibliography **81**

Appendix A: DC fan volumetric flow determination **83**

Appendix B: CFD turbulence models coefficients calculation **87**

Appendix C: Newton's method **91**

Nomenclature

Variable	Name	Unit
A	Area	m^2
C_p	Specific heat	$J/kg \cdot K$
D	Diameter	m
d	Base thickness	m
E	Energy	-
F	Force	N
f	Friction factor	-
G	Generation	-
H	Height	m
h	Convective heat transfer coefficient	$W/(m^2 \cdot K)$
I	Current	A
k	Turbulence kinetic energy	-
k_s	Sand equivalent roughness	mm
L	Length	m
l_c	Contact resistance thickness	m
m	Mass	kg
$\dot{m}$	Mass flow	kg/s
n	Electric contact parameter	m
N	Number of elements	-
Nu	Nusselt number	-
P	Electrical power	W
p	Pressure	Pa
Pr	Prandtl number	-
r	Thermal contact parameter	-
R	Electrical resistance	Ω
Re	Reynolds number	-

S	Source	W/m^3
s	Separation	m
T	Temperature	K
t	Time	s
u	Velocity	m/s
V	Voltage	V
W	Width	m
$\dot{Q}$	Heat flux	W
$\dot{q}$	Volumetric flow	m^3/s
α	Seebeck coeficient	V/K
Γ	Diffusivity	-
δ	Thickness	m
η	Efficiency	-
λ	Thermal conductivity	$W/(m \cdot K)$
μ	Dynamic viscosity	Pa/s
μ_t	Turbulent viscosity	-
ν	Kinematic viscosity	m^2/s
ρ	Density	kg/m^3
σ	Electrical conductivity	S/m
τ	Stress tensor	-
θ	Thermal resistance	K/W
ω	Specific dissipation rate	-

Subscript	
cer	Ceramic
ch	Channels
cold	Cold side
comp	Compressor
cond	Conduction
conv	Convection
eff	Effective
E	Energy
f	Fins
fan	Fan
heat	Heat
hot	hot side
HS	Heat sink
HX	Heat exchanger
int	Internal
load	Electrical load
mat	Material
m	MAss
pump	Pump
TEG	Thermoelectric Generator
trans	Transition
turb	Turbulent

Acronym	
DC	Direct Current
HS	Heat Sink
HSHX	How Side Heat Exchanger
HX	Heat Exchanger
TEG	Thermoelectric Generator
WHR	Waste Heat Recovery
WHRS	Waste Heat Recovery System

Chapter 1

Introduction

Thermoelectric generators (TEGs) are devices that convert heat directly into electricity. Their working principle is the same as a thermal engine, this is operating between a heat source and a heat sink, converting part of the heat source in work and rejecting the rest to the sink. TEGs present distinct advantages compared to conventional thermal engines: they have no moving parts, are reliable and noiseless devices with low or null maintenance, and are able to operate over a wide range of transient temperature conditions [Stevens et al., 2014]. On the other hand, their high cost and poor efficiency so far have reduced their implementation [Stevens et al., 2014]. However, for waste heat recovery (WHR) applications where a conventional thermal engine cannot be used this technology is considered, because its efficiency is not a big drawback, since the heat source is waste heat.

The auto-mobile industry has shown a growing interest on the implementation of TEG technology in order to recover waste heat from the vehicle engine [General Motors, 2011]. As can be seen in the Sankey diagram in Figure 1.1, just a 30 % of the combusted fuel is transferred to the shaft. From this fraction, a 5 % is used to overcome the friction losses and just a 25 % represents a net use for the car mobility and accessories [Wang et al., 2013]. The rest is transferred to the engine coolant and rejected to the atmosphere as exhaust gas. On the other hand, there is an on-board electric load, provided by the car alternator. It varies from 160 W for a small size car to 500 W for a full size truck [General Motors, 2011]. Therefore, the exploitation of the waste heat in order to substitute or reduce the alternator load leads to the following benefits: improved vehicle fuel efficiency, lower CO2 emissions and support the vehicle electrification [General Motors, 2011].

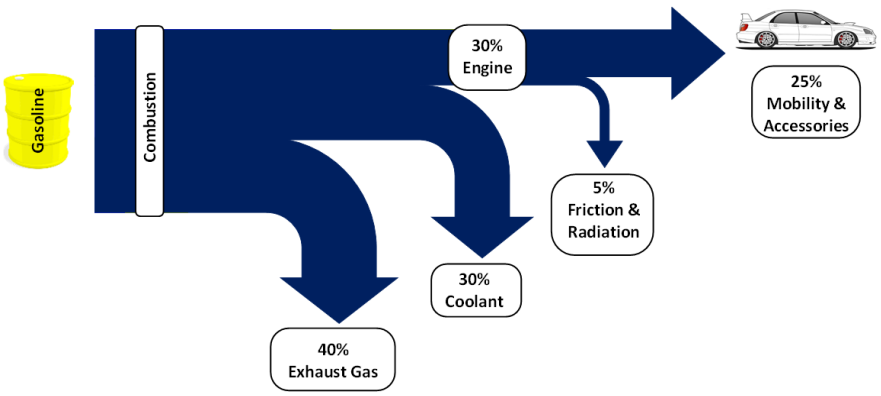

Figure 1.1: Car diesel engine Sankey diagram.

In this project, a TEG based waste heat recovery system (WHRS) for automotive applications is described and discussed. In the next sections, the working principle of a TEG and the considered aspects in the design of the WHRS are described. In addition, the followed methodology is presented.

1.1 Thermoelectric materials and their properties

Thermoelectric materials are semiconductors with a particular characteristic: the material electrons release their bonds when there is a heat flux across the material [Tellurex, 2006].

Each atom of semiconductor material consists on a core made of protons (positive charge) and neutrons (no charge on them) surrounded by electrons (negative charge). The individual atoms are attached to each other by covalent bonds. This bond consist of two atoms sharing a single electron [Honsberg and Bowden, 2014]. Although silicon is not a thermoelectric material, it is a well known semiconductor material and it is used to show the covalent bonds in a crystal lattice, represented in figure 1.2.

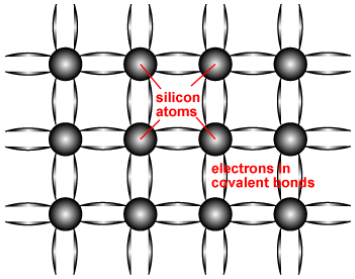

Figure 1.2: Representation of covalent bonds in a silicon crystal lattice [Honsberg and Bowden, 2014].

When the semiconductor electrons receive a certain amount of energy, they leave the bonds and set in motion. When an electron leaves its bond, there is a free space on it called 'hole'. The electron next to the free electron moves and occupies the hole, leaving behind a new hole. Therefore the hole is considered as the move of a positive charge. Both electron and hole participate in conduction and are called 'carriers'. Depending on the relative amount of the two carriers, they can be designed as majority or minority carriers [Honsberg and Bowden, 2014].

In practice, dopants are added to the semiconductor, this leads to a different majority carrier type concentration. Two types or semiconductors are obtained depending on the dopant: n and p type. In the n type, the electrons are the majority carrier while the holes are the majority carrier in the p type. The covalent bond in a p and n doped silicon crystal lattice can be seen in Figure 1.3.

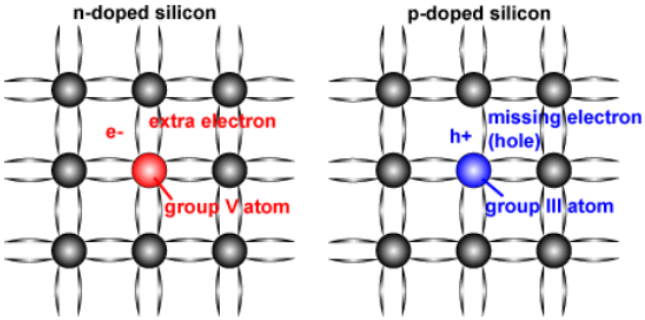

Figure 1.3: Representation of covalent bonds in p and n doped silicon crystal lattice [Honsberg and Bowden, 2014].

In thermoelectric materials, a heat flow provides the energy required to set the electrons free. This phenomena can even take place in conductors. In practice, conductor materials are used in temperature measurement. A probe made of metal or a metal alloy, called thermocouple, is used. It generates a small voltage between

its terminals proportional to the temperature of the environment where it is placed because of the Seebeck effect [Rowe, 2005].

The thermocouples for temperature measurement have a Seebeck coefficient around tens of micro-volts per temperature degree, however Seebeck coefficient around hundreds of micro-volts can be achieved by the use of semiconductor materials whose properties have been specially developed to achieve Seebeck coefficients specifically for power generation [Rowe, 2005].

The most commonly used semiconductor material alloys are based on Bismuth in combination with Antimony, Tellurium and Selenium. They are considered as low-temperature materials since they can be used in applications with a maximum temperature around 450 K (177 ° C). Semiconductor alloys based on lead Telluride can operate up to 850 K (577 ° C) while those based on Silicon Germanium alloys can operate up to 1300 K (1027 ° C) [Rowe, 2005].

Both p and n type thermoelectric pellets are manufactured. The reason for manufacturing different thermoelectric pellets is that the polarity of the generated voltage is different. This is illustrated in Figure 1.4 where a voltmeter is connected between the terminals of a pellet subject to a temperature gradient.

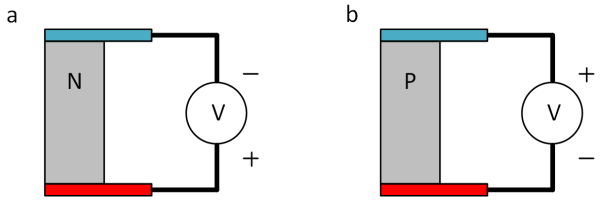

Figure 1.4: a) N type thermoelectric pellet. b) P type thermoelectric pellet.

Since the voltage in each pellet has opposite polarity, the electrons flow in opposite direction since they flow from the higher to the lower potential. To obtain useful voltage levels, n and p type pellets are connected electrically in series and thermally in parallel as shown in Figure 1.5. The polarity of the generated voltage in each pellet is drawn on it. If pellets of the same type were used and the generated voltage in each pellet were the same, the net voltage output would be zero.

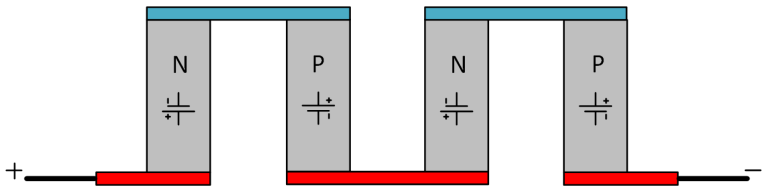

Figure 1.5: Performance of two thermoelectric n-p couples in series.

If same type pellets were used, they should be connected as shown in Figure 1.6 to obtain a voltage difference between the positive and negative terminal of the

module. This would lead to a more complex manufacturing and larger connection tabs.

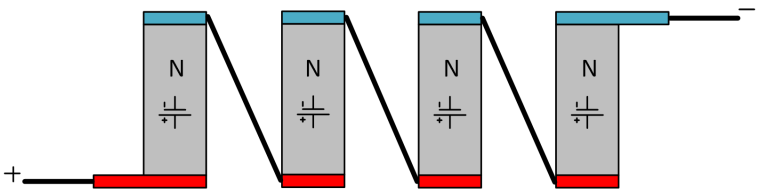

Figure 1.6: Performance of two thermoelectric n-n couples in series.

The array of pellets is placed between two plates forming a module. The plates provide mechanical strength and insulation to the pellets, they are made of ceramic material since offers the best compromise between mechanical strength, electrical resistivity and thermal conductivity [Tellurex, 2006]. A TEG module can be seen in Figure 1.7.

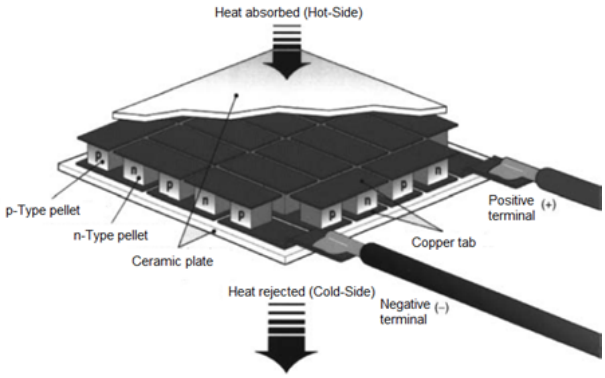

Figure 1.7: TEG module and its performance [Rowe, 2005].

1.2 Problem definition

In this project, a TEG based WHRS for automotive applications has to be optimized.

The heat is transferred from the engine exhaust gas to the TEG through a heat exchanger (HX). It consists on a rectangular duct connected to the automobile exhaust gas pipe. The TEG module hot side is placed on its outer surface.

The efficiency of the TEG depends on the material properties and the temperature gradient across it. Therefore a heat sink (HS) is attached on its cold side to obtain an appropriate temperature gradient [Tellurex, 2006]. The possibility of implementing both water and air cooling is examined. The considered heat sink consists on an array of channels where the cooling fluid flows through, while the air cooling system

consist on a fin plate heat sink with a fan attached to the HS top. An overview of the proposed waste heat recovery system can be seen in Figure 1.8.

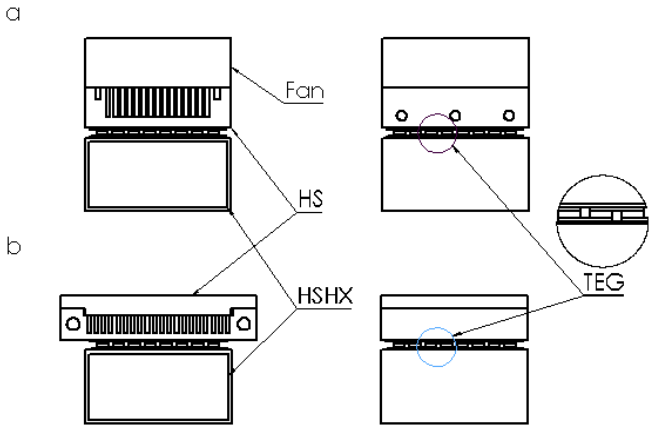

Figure 1.8: Proposed waste heat recovery system. a) Air cooled. b) Water cooled.

To optimize the TEG power generation, the thermal resistance of the TEG and the WHRS heat exchanger network have to be matched to produce the highest possible power [Baranowski et al., 2013]. In figure 1.9 the power generated versus the ratio between the TEG and the heat exchangers thermal resistance can be seen.

The HX and HS thermal resistance depends on its geometry, the material used on its construction and the fluid velocity [Çengel, 2003]. Therefore an optimal design has to be found for the heat exchangers to ensure the TEG maximum energy production, while minimizing the cooling power consumption.

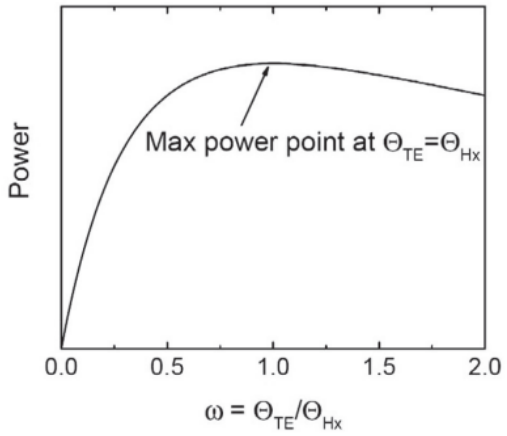

Figure 1.9: TEG power production as a function of the TEG/HX thermal resistance ratio [Baranowski et al., 2013].

1.3 Methodology

A steady state model is developed in order to predict the behaviour of the WHRS. It is developed both in MATLAB, based on analytical equations and in the Computational Fluid Dynamics (CFD) software FLUENT which is based on the continuity, momentum and energy equations. This is made in order to compare their accuracy. In addition, the models are validated with laboratory test. A experimental setup was designed and manufactured. The experimental validation was performed in the thermoelectric laboratory at Aalborg University.

Finally a WHRS optimal design, in order to maximize the net power production, was obtained from the analytical model and the net power production of the optimal WHRS was predicted.

Chapter 2

Analytical model

In this section, the elements that form the WHRS are introduced. These elements are the heat exchangers and the thermoelectric module. The governing equations used to develop the analytical model are described.

2.1 TEG module electric model

The TEG module is the core of the WHRS. It converts heat directly in electricity when there is a temperature gradient across it. Its electric model is described in this section.

The TEG module generates a voltage V_α proportional to the temperature gradient, according to Equation 2.1, where N_{legs} is the number of thermoelectric pellets and α is the Seebeck coefficient, which is a thermoelectric property of the material.

$$V_\alpha = \frac{N_{legs}}{2} \cdot \alpha \cdot \Delta T \tag{2.1}$$

When a load is connected between the module terminals, a DC current is originated. The current provided by the TEG module can be computed by applying Ohm's law to its equivalent circuit, represented in Figure 2.1. As can be seen in Equation 2.2, the current is inversely proportional to the load value, as the power provided to the load as seen

$$I = \frac{V_\alpha}{R_{int} + R_{load}} \tag{2.2}$$

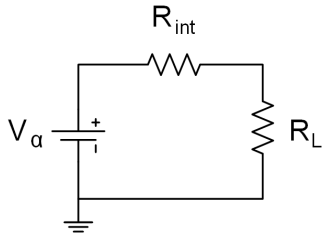

Figure 2.1: TEG module equivalent electric circuit.

The electric resistance R_{int} represents the internal resistance of the module and is computed according to Equation 2.3, where σ is the electrical conductivity of the thermoelectric material.

$$R_{int} = N_{legs} \cdot \frac{l_{legs}}{A_{legs} \cdot \sigma} \tag{2.3}$$

The existence of the module thermal resistance implies that when a load is connected, the voltage provided to the load is lower than V_α.

The maximum electrical efficiency takes place when the load is equal to the module thermal resistance [Tellurex, 2006]. Therefore it is assumed that the electric load is equal to the module internal resistance. With this assumption, and introducing Equations 2.1 and 2.3 in equation 2.2 leads to Equation 2.4.

$$I = \frac{A_{legs} \cdot \sigma \cdot \alpha \cdot \Delta T}{4 \cdot N_{legs} \cdot L_{legs}} \tag{2.4}$$

The power provided by the TEG to the load is computed according to equation 2.5.

$$P_{load} = I^2 \cdot R_{load} \tag{2.5}$$

Since it has been assumed the load electric resistance matches with the internal resistance, introducing Equations 2.3 and 2.4 into Equation 2.5 leads to Equation 2.6

$$P_{load} = \frac{A_{legs} \cdot N_{legs} \cdot \sigma \cdot (\alpha \cdot \Delta T)^2}{8 \cdot l_{legs}} \tag{2.6}$$

The TEG electrical model described above lead to Figure 2.2 and Figure 2.3 for TEG and temperature literature data [Bitschi, 2009]. As can be seen, the voltage provided to the load decreases with the current and the power provided to the load has its maximum value when the load and the internal resistance are matched.

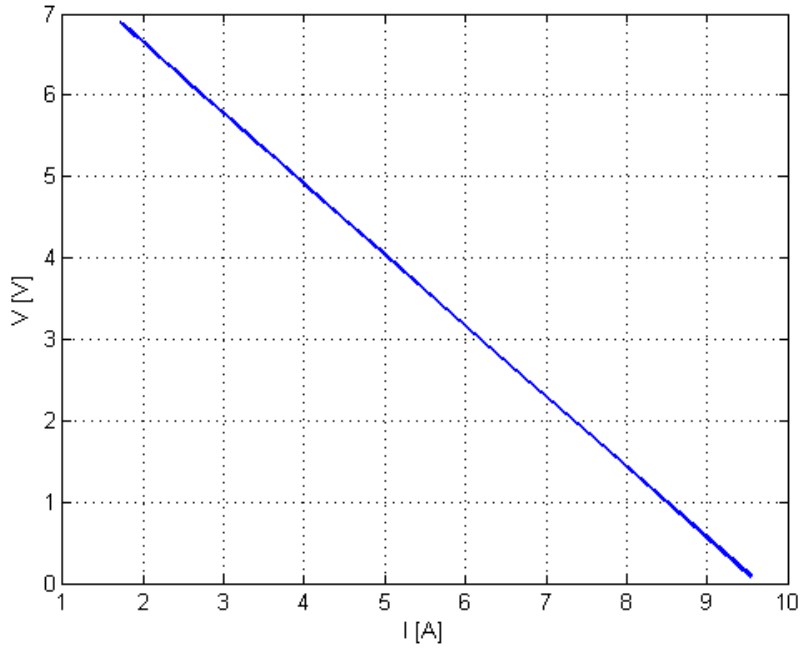

Figure 2.2: TEG module V-I curve.

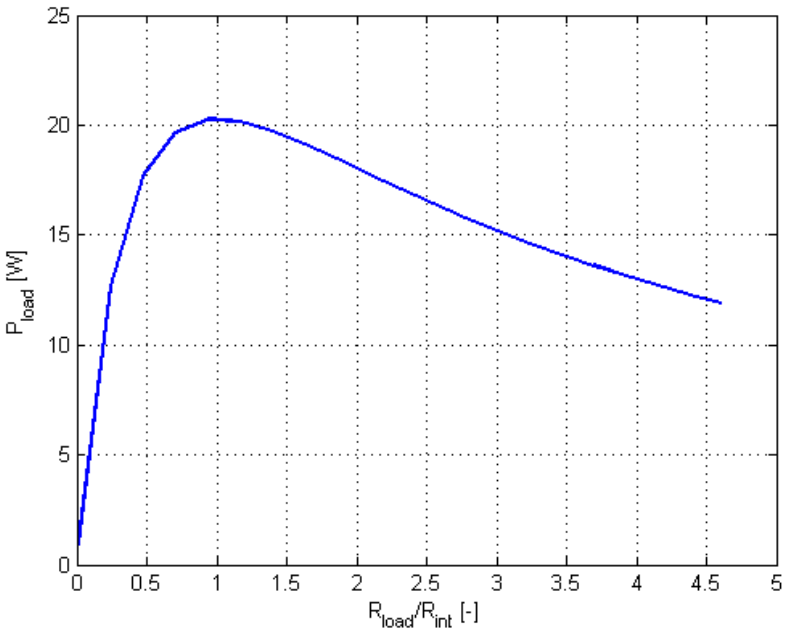

Figure 2.3: Power provided to the load as a function of the ratio between load and internal resistance.

As seen in Equation 2.6, the power generation is a function of the temperature gradient across the TEG, the thermoelectric material properties and the dimensions of the legs. The derived equation has been proved to be adequate for analysis of large-dimension thermoelectric modules, however it becomes inaccurate and sometimes invalid for short legs length [Min, 2005]. The effect of the electric and thermal contact resistances is included since the legs are relatively short, when the module has been designed to maximize the power generation. Since in this project short legs length values are used, Equation 2.7 is used [Min, 2005].

$$P_{load} = \frac{A_{legs} \cdot N_{legs} \cdot \sigma_{legs} \cdot (\alpha \cdot \Delta T)^2}{8 \cdot (n + L_{legs}) \cdot (1 + 2 \cdot r \cdot \frac{l_c}{L_{legs}})^2} \tag{2.7}$$

2.2 WHRS thermal model

From the previous section, it is clear that the generated power is directly proportional to the square of the temperature gradient across the module. Therefore the heat exchangers used to conduct the heat through the TEG module play a crucial role in this project.

Each of the elements of the WHRS are characterized by a thermal resistance value. When a heat flows across a thermal resistance, a temperature gradient is produced. The temperature gradient between a thermal resistance can be calculated using Equation 2.8 [Çengel, 2003].

$$\Delta T = \dot{Q} \cdot \theta \tag{2.8}$$

This calculation is analogous to apply Ohm's law to an electric circuit, as it was done in Section 2.1. Voltage drop, electric resistance and electric current are related in the same way as temperature gradient, thermal resistance and heat flow.

The heat transfer in the modelled WHRS is represented in the equivalent thermal circuit shown in Figure 2.4.

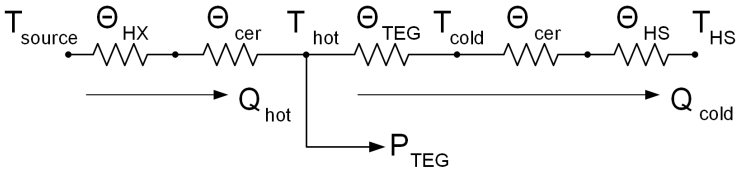

Figure 2.4: WHRS equivalent thermal circuit.

Where θ_{HX} is the hot side heat exchanger (HSHX) thermal resistance, θ_{cer} is the ceramic plate thermal resistance, θ_{TEG} is the pellets thermal resistance and θ_{HS} is

the HS thermal resistance. All of them will be described in detail during the following subsections.

T_{source} is the temperature of the heat source and T_{HS} is the temperature of the HS cooling fluid, while T_{hot} and T_{cold} are the temperature at both sides of the TEG pellets. Finally $\dot{Q}_{hot}$ is the amount of heat entering the TEG module and $\dot{Q}_{cold}$ is the amount leaving it and are computed according to Equation 2.9 and Equation 2.10 [Stevens et al., 2014], respectively. The difference between them is the electrical power provided to the load.

$$\dot{Q}_{hot} = \alpha \cdot I \cdot T_{hot} + \frac{T_{hot} - T_{cold}}{\theta_{TEG}} - \frac{1}{2} \cdot I^2 \cdot R_{int} \tag{2.9}$$

$$\dot{Q}_{cold} = \alpha \cdot I \cdot T_{cold} + \frac{T_{hot} - T_{cold}}{\theta_{TEG}} + \frac{1}{2} \cdot I^2 \cdot R_{int} \tag{2.10}$$

The terms within the previous equations represent, from left to right, the generated power by the TEG, conduction heat transfer across the TEG and Joule effect losses in the internal resistance. The internal resistance has to account for the contact resistance.

Now the thermal circuit heat fluxes are defined, T_{hot} and T_{cold} are calculated according to Equation 2.11 and 2.12, respectively.

$$T_{hot} = T_{source} - \dot{Q}_{hot} \cdot (\theta_{HX} + \theta_{cer}) \tag{2.11}$$

$$T_{cold} = T_{HS} + \dot{Q}_{cold} \cdot (\theta_{HS} + \theta_{cer}) \tag{2.12}$$

2.2.1 TEG module thermal model

As previously introduced, a TEG module consists on an array of thermoelectric pellets connected electrically in series and thermally in parallel. The pellets are placed between two ceramic plates that provide mechanical strength and electrical isolation to the pellets.

The geometry and the thermal properties of the materials determines the resistance the module shows against the heat transfer across it due to conduction. The conduction thermal resistance is computed according to Equation 2.13 and will be used in this and in the following subsections.

$$\theta_{cond} = \frac{\delta}{\lambda_{mat} \cdot A} \tag{2.13}$$

where δ is the thickness of the element, λ is its thermal conductivity and A is its area. In addition, the contact resistance effect has to be included to compute the TEG thermal resistance, which leads to Equation 2.14.

$$\theta_{cond} = \frac{L_{legs}}{N_{legs} \cdot A_{legs} \cdot \lambda_{TEG} \cdot (1 + 2 \cdot r \cdot \frac{l_c}{L_{legs}})} \tag{2.14}$$

2.2.2 Hot side heat exchanger model

The exhaust gas waste heat is transferred to the TEG module by a HX. Its thermal resistance is composed by a conduction and a convection term, as sated in Equation 2.15.

$$\theta_{HX} = \theta_{conv} + \theta_{cond} \tag{2.15}$$

The conduction thermal resistance is computed according to Equation 2.13. The convection term represents the effect of the fluid motion when it flows across the heat exchanger and is calculated according to Equation 2.16.

$$\theta_{conv} = \frac{1}{A \cdot h} \tag{2.16}$$

The convective heat transfer coefficient h is calculated using the Nusselt number of the fluid according to Equation 2.17.

$$h = \frac{Nu \cdot \lambda_{fluid}}{D_H} \tag{2.17}$$

Where D_h is the hydraulic diameter of the duct and is computed according to Equation 2.18 [Crowe, 2010], where p is the perimeter of the duct cross section area.

$$D_h = \frac{4 \cdot A}{Perimeter} \tag{2.18}$$

In order to determine the flow regime of the fluid, the Reynolds number is computed according to Equation 2.19 as a function of the velocity and viscosity of the fluid and the hydraulic diameter of the duct the fluid is flowing through .

$$Re = \frac{u_{fluid} \cdot D_H}{\nu_{fluid}} = \frac{u_{fluid} \cdot D_H \cdot \rho_{fluid}}{\mu_{fluid}} \tag{2.19}$$

The Nusselt number of the fluid is computed by an empirical relation known as Gnielinski correlation. An expression for both laminar and turbulent flow can be found in [Gnielinski, 2010]. This relations will be used as well in the HS model.

For Reynolds number values lower than 2300 the fluid flow regime is considered laminar and its Nusselt number is computed according to Equation 2.20 [Gnielinski, 2010].

$$Nu_{laminar} = \sqrt[3]{7.541^3 + 1.841^3 \cdot \frac{Re \cdot Pr \cdot D_h}{L}} \tag{2.20}$$

When the fluid Reynolds number surpass 2300, the first turbulence appears. The flow experiences a transition between laminar and turbulent until a Reynolds number of 10000 is achieved [Gnielinski, 2010]. Therefore when $2300 < Re < 10000$ the Nusselt number is computed according to Equation 2.21 [Gnielinski, 2010].

$$Nu_{trans} = (1 - \gamma) \cdot Nu_{lam,2300} + \gamma \cdot Nu_{turb,10^4} \tag{2.21}$$

where $Nu_{lam,2300}$ is the Nusselt number for laminar flow at a Reynolds number of 2300, $Nu_{turb,10^4}$ is the Nusselt number for a turbulent flow at a Reynolds number of 10000 and γ is a coefficient calculated according to Equation 2.22.

$$\gamma = \frac{Re - 2300}{10^4 - 2300} \tag{2.22}$$

The fluid flows in fully developed turbulent regime when it has reached a Reynolds number of 10000 and its Nusselt number is computed according to Equation 2.23 [Gnielinski, 2010].

$$Nu_{turb} = \frac{(\xi/8) \cdot Re \cdot Pr}{1 + 12.7\sqrt{\xi/8} \cdot (Pr^{2/3} - 1)} \cdot (1 + (\frac{D_h}{L})^{2/3}) \tag{2.23}$$

where

$$\xi = (1.8 \cdot \log Re - 1.5)^{-2} \tag{2.24}$$

As seen, the relations developed by Gnielinski depend on the length of the duct, the fluid Reynolds number and the Prandtl number Pr. The Prandtl number entirely depends on the properties of the fluid as seen in Equation 2.25.

$$Pr = \frac{C_{p,fluid} \cdot \mu_{fluid}}{\lambda_{fluid}} \tag{2.25}$$

Approximating the exhaust gas to air, the HSHX model provides the following results for a fixed HSHX geometry and a variable exhaust gas mass flow rate. Figure 2.5 shows the variation of the fluid Nusselts number as a function of the Reynolds number for the given conditions, while the variations of the HSHX thermal resistance as a function of the Reynolds number can be seen in Figure 2.6. As seen in Figure 2.6, the thermal resistance due to conduction is much smaller than the thermal resistance due to convection, therefore it can be neglected.

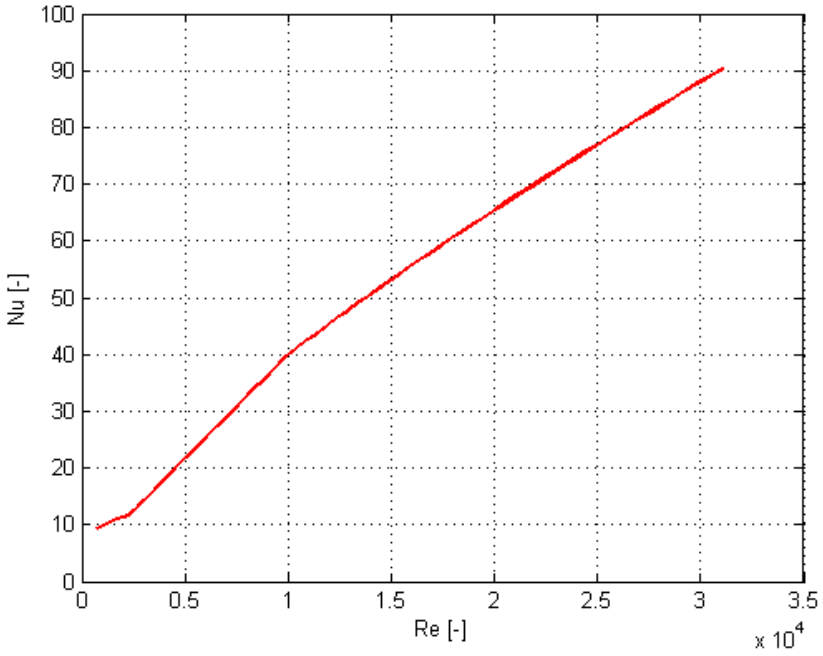

Figure 2.5: Exhaust gas Nusselt number as a function of its Reynolds number.

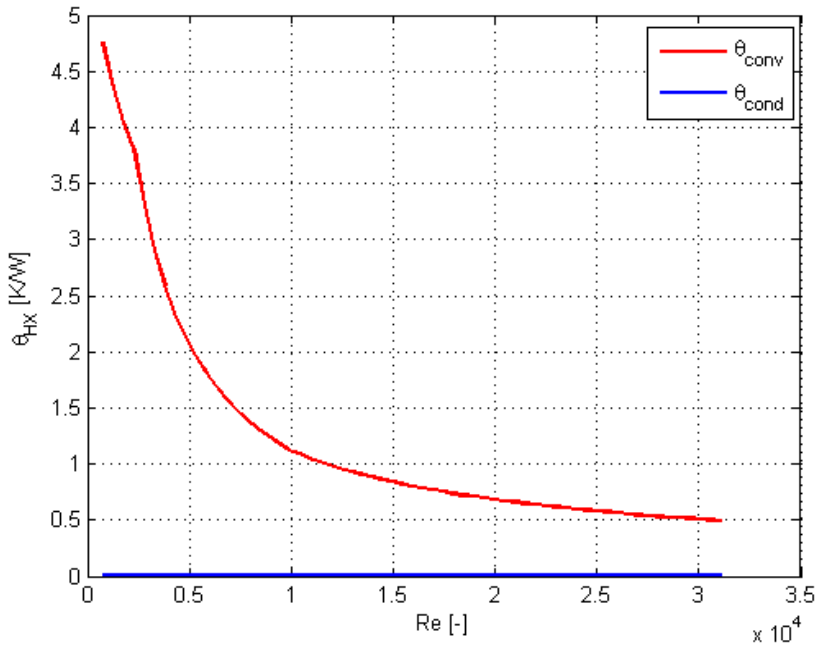

Figure 2.6: Hot side heat exchanger thermal resistance as a function of the exhaust gas Reynolds number.

2.2.3 Heat sink model

A heat sink is used to obtain an optimal ΔT across the TEG and to reject the remaining heat to a cooling fluid. Both water and air heat sinks are considered as possible candidates.

Water heat sink

The water heat sink (WHS) is approached as an arrange of channels where the cooling water flows through them. The considered heat sink is shown in Figure 2.7, where the geometrical parameters used in the equations presented in this subsection are labelled.

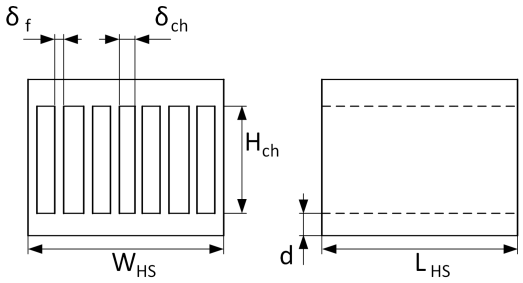

Figure 2.7: Water heat sink sketch.

Its equivalent thermal resistance is computed according to Equation 2.26.

$$\theta_{HS} = \theta_{cond} + \theta_{heat} + \theta_{conv} \tag{2.26}$$

The conduction thermal resistance for the given geometry in Figure 2.7 is calculated according to Equation 2.27.

$$\theta_{cond} = 2 \cdot \theta_{base} + \theta_{walls} \tag{2.27}$$

where θ_{base} and θ_{walls} are respectively the base and walls thermal resistance and are computed according to Equation 2.28 and 2.29.

$$\theta_{base} = \frac{d}{\lambda_{mat} \cdot L_{HS} \cdot W_{HS}} \tag{2.28}$$

$$\theta_{walls} = \frac{H_{ch}}{\lambda_{mat} \cdot L_{HS} \cdot \delta_f \; n_f} \tag{2.29}$$

The heat resistance represent the cooling fluid temperature increase produced as it flows through the channels and is computed according to Equation 2.30 [Tuckerman and Pease, 1981].

$$\theta_{heat} = \frac{1}{\dot{m} \cdot c_p} \tag{2.30}$$

Where $\dot{m}$ is the mass flow rate of the cooling fluid and is calculated according to Equation 2.31 [Rezania et al., 2013].

$$\dot{m} = \rho \cdot N_{ch} \cdot \delta_{ch} \cdot H_{ch} \cdot u_{fluid} \tag{2.31}$$

The thermal resistance due to convection has been previously defined. However the HS convection thermal resistance varies from Equation 2.16 since a term standing by the efficiency of the walls is introduced, as seen in Equation 2.32 [Tuckerman and Pease, 1981].

$$\theta_{conv} = \frac{1}{\eta_f \cdot h \cdot A_{ch}} \tag{2.32}$$

This term is introduced since the temperature difference between the cooling fluid and the wall varies through the wall height. An analytical approximation for the fin efficiency is seen in Equation 2.33. [Tuckerman and Pease, 1981].

$$\eta_f = \frac{\tanh\left(\sqrt{\frac{2 \cdot h}{k_{fluid} \cdot H_{ch} \cdot \delta_f}} \cdot H_{ch}\right)}{\sqrt{\frac{2 \cdot h}{k_{fluid} \cdot H_{ch} \cdot \delta_f}} \cdot H_{ch}} \tag{2.33}$$

The area of the channels A_{ch} can be expressed as the product of the channels cross section perimeter, their length and the number of channels according to Equation 2.34.

$$A_{ch} = 2 \cdot N_{ch} \cdot (\delta_{ch} + H_{ch}) \cdot L_{HS} \tag{2.34}$$

The set of equations defining the water heat sink model lead to the following results for a fixed HS geometry and variable water velocity: in Figure 2.8 the Nusselt number of the water is plotted as a function of its Reynolds number, while in Figure 2.9 the thermal resistance of the WHS can be seen as a function of the fluid Reynolds number. Both figures were produced by introducing literature data in the equations above.

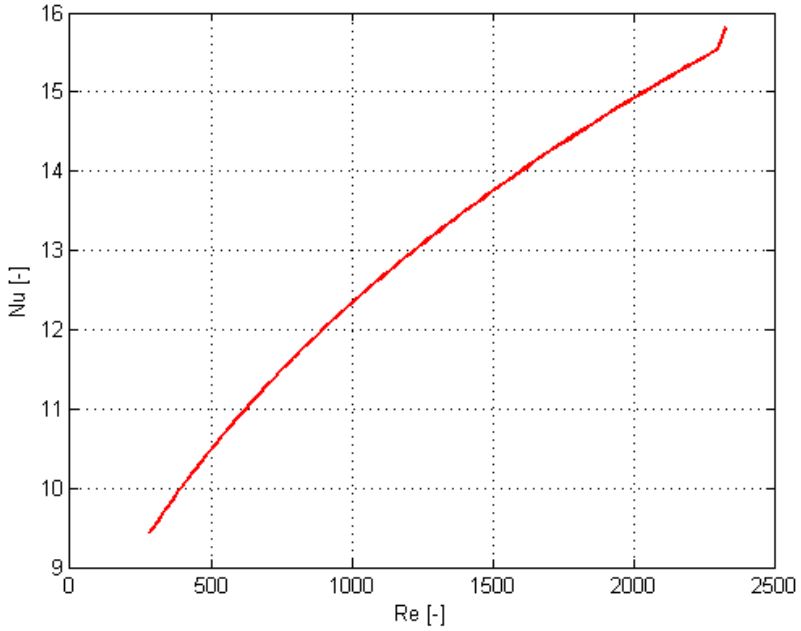

Figure 2.8: Cooling water Nusselt number as a function of its Reynolds number.

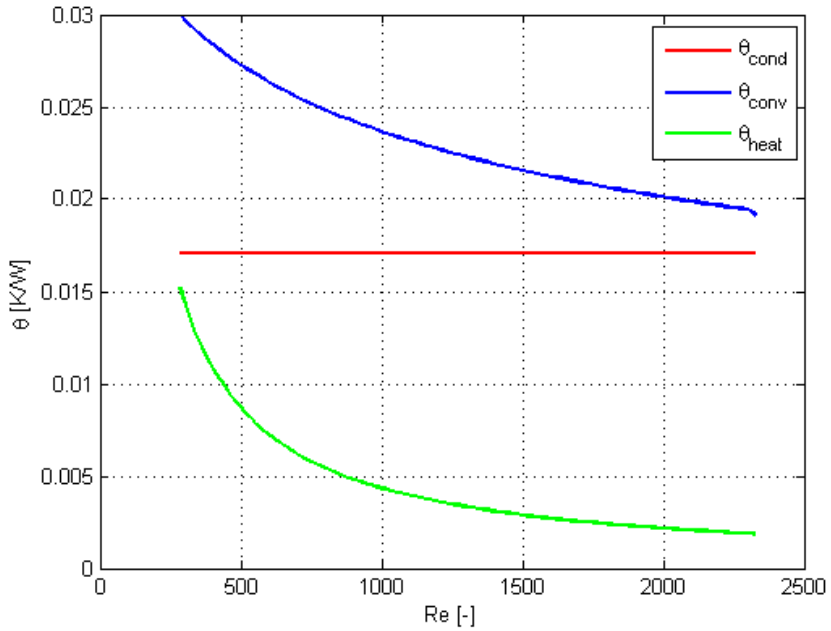

Figure 2.9: Heat sink thermal resistance as a function of the cooling water Reynolds number.

On the other hand, the pumping power of the heat sink can be computed as the product of the total volumetric flow and the pressure losses along the channels.

$$P_{pump} = N_{ch} \cdot \delta_{ch} \cdot H_{ch} \cdot u_{fluid} \cdot \Delta P \tag{2.35}$$

The pressure loss in each of the heat sink channels is calculated using the Darcy-Weisbach equation, state in Equation 2.36 [Crowe, 2010]. If the inlet and outlets of the heat sink were considered, the influence of the convergent/divergent sections and bending ducts should be taken into account.

$$\Delta p = f \cdot \frac{L \cdot u_{fluid}^2}{D_h \cdot 2} \cdot \rho \tag{2.36}$$

Where the friction factor f depends on the Reynolds number and the flow regime. For laminar flow it is defined as $\frac{64}{Re}$ [Crowe, 2010]. In addition, a friction factor of $\frac{48}{Re}$ is considered for laminar flow across channels on the micro-scale [Tuckerman and Pease, 1981]. This is, channels with a hydraulic diameter smaller than 1 mm. However, the friction factor for turbulent flow calculation is not so straight forward and Equation 2.37 is used [Crowe, 2010].

$$f = \frac{0.25}{(log_{10}(\frac{k_s}{3.7 \cdot D_h} + \frac{5.74}{Re^{0.9}}))^2} \tag{2.37}$$

Air heat sink

The heat sink consists on a fin plate in order to increase the heat exchange surface. In addition, a DC fan is attached to the top to enhance the heat transfer rate by increase the speed of the air. A sketch of the fin plate heat sink can be seen in Figure 2.10

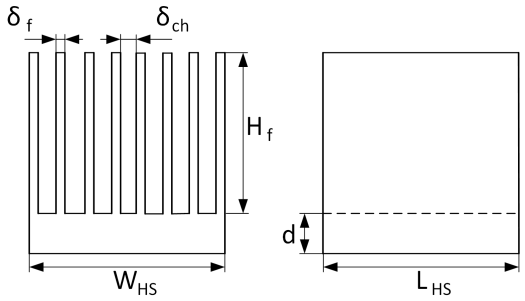

Figure 2.10: Fin plate heat sink sketch.

Its thermal resistance is computed according to Equation 2.38.

$$\theta_{HS} = \theta_{cond} + \theta_{conv} + \theta_{heat} \tag{2.38}$$

The conduction term is calculated according to Equation 2.39.

$$\theta_{cond} = \theta_{base} + \theta_{fins} \tag{2.39}$$

θ_{base} is calculated according to Equation 2.28 and θ_{fins} are calculated as θ_{walls} according to Equation 2.29.

The convection thermal resistance is calculated as in previous sections, as a function of the area in contact with the cooling fluid and its Nusselt number. The empirical relations developed by Gnielinski are used once again.

To compute the Reynolds number, the velocity of the cooling fluid is required. It is calculated using the volumetric flow value provided by the DC fan $\dot{q}$ and the cross section area of the HS channels according to Equation 2.40.

$$u_{fluid} = \frac{\dot{q}}{L \cdot \delta_{ch} \cdot n_{ch}} \tag{2.40}$$

Finally the heat thermal resistance can be stated as in Equation 2.41.

$$\theta_{heat} = \frac{1}{\rho_{air} \cdot C_{p,air} \cdot \dot{q}} \tag{2.41}$$

The model leads to the following values for a given geometry and a variable volumetric flow. The fluid Nusselt number can be seen as a function of its Reynolds number in Figure 2.11, while in Figure 2.12 the thermal resistance of the heat sink can be seen as a function of the fluid Reynolds number. Both figures were produced by introducing literature data in the equations above. On the other hand, the power consumption of the DC fan can be calculated analogously to the pump consumption, as seen in Equation 2.42.

$$P_{fan} = \Delta p \cdot \dot{q} \tag{2.42}$$

The pressure loss within the heat sink geometry is computed with Equation 2.36, where the friction coefficient is calculated as in the water heat sink case.

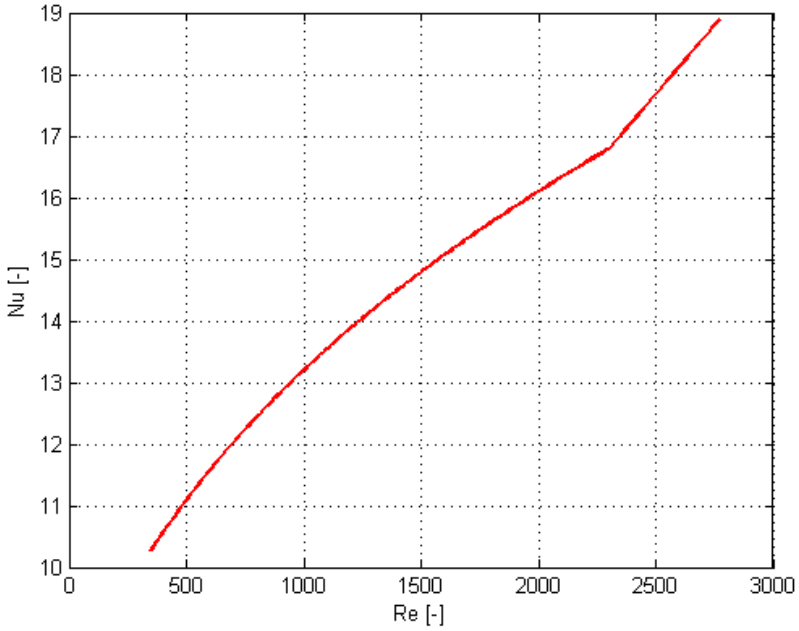

Figure 2.11: Cooling air Nusselt number as a function of its Reynolds number.

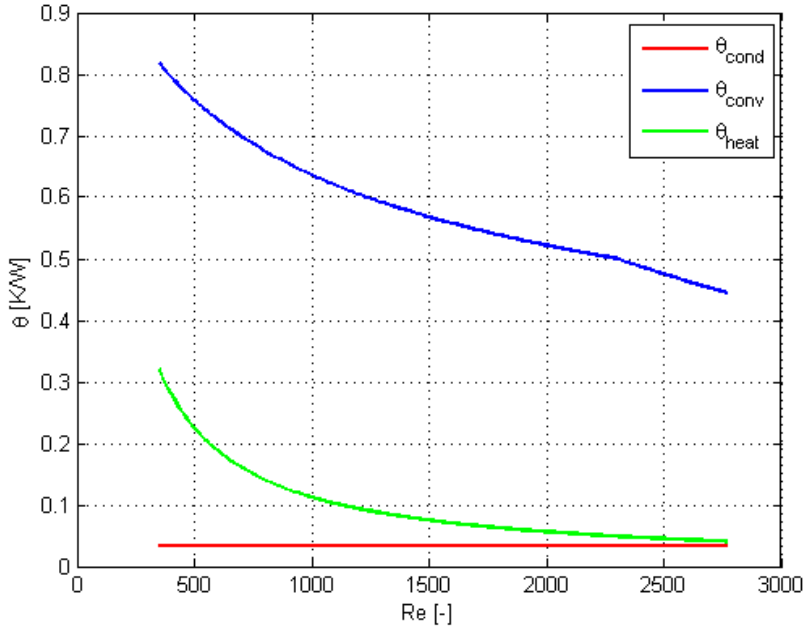

Figure 2.12: Heat sink thermal resistance as a function of the cooling air Reynolds number.

Chapter 3

Experimental validation

3.1 Experimental setup description

In this chapter the experimental setup used to test the proposed WHRS is described. The setup mainly consists on the elements described in Chapter 2. This is the hot side heat exchanger, a TEG module, and the HS. In Figure 3.1 an overall view of the setup is given.

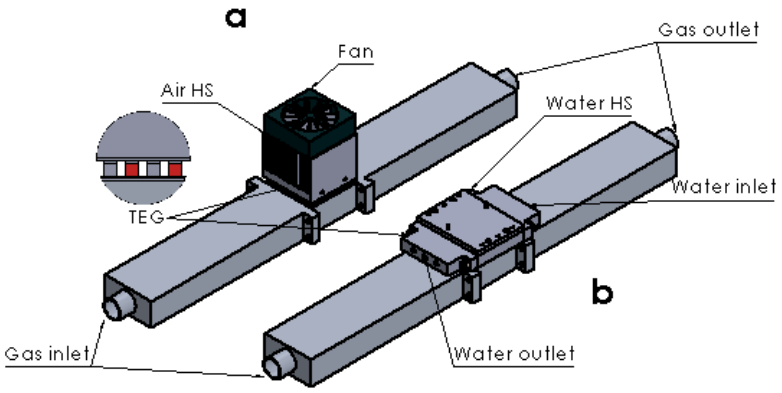

Figure 3.1: a) Air cooled waste heat recovery system. b) Water cooled waste heat recovery system.

3.1.1 Hot side heat exchanger design

Hot air coming from the laboratory exhaust gas simulator is circulated through the hot side heat exchanger.

The heat exchanger was initially designed as seen in figure 3.2, however some problems with the machinery that was going to manufacture it made not possible its fabrication.

The initial designed consisted on three different parts: inlet, outlet and the heat exchanger itself.

The inlet piece was going to be used to smoothly increase the section of the exhaust gas simulator pipe size (20 mm) until a plate big enough to place the TEG module is obtained. The inlet is a diverging pipe with a diffuser expansion angle. Sparrow et al. [2009] showed that flow separation did not occur for this diffuser expansion angle of 5°. The diffuser expansion angle of the inlet and outlet part was designed in order to obtain an angle close to 5°. Figure 3.2 shows the initial design of the HSHX.

The outlet was going to be constructively equal, converging from the heat exchanger section to the exhaust gas cross section area. The heat exchanger was designed as an aluminium pipe with a rectangular cross section area. Its dimensions had been set to $30 \times 60 \times 60$ mm. The TEG module has to be placed on its surface.

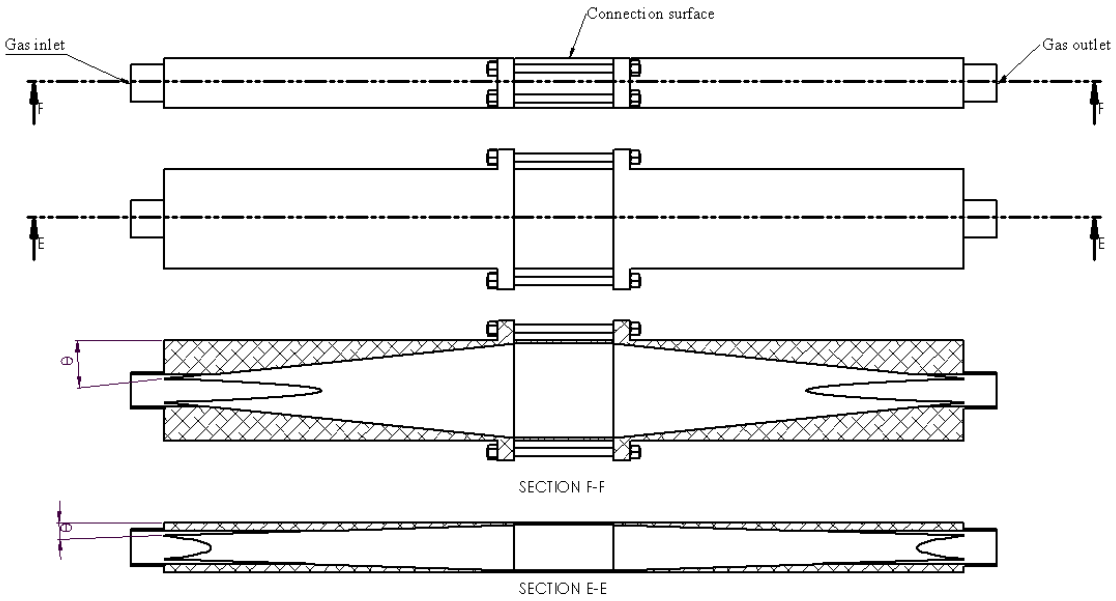

Figure 3.2: Experimental Hot side heat exchanger section cut

The initial design shown in Figure 3.2 was not possible to be manufactured and therefore a much simpler geometry has to be built. Instead, a rectangular duct with 30×60 section was used as the HX. A grid with orifices in it was placed inside the duct in order to increase the fluid pressure losses and thus decrease the required development length of the fluid. If this grid would not have been placed, the entrance length of the fluid had been much higher.

The flow coming out of the exhaust gas simulator pipe is a high turbulent jet. It can be approximated as a nearly conical flow shape with an angle of 11.8°. Therefore the grid has to be placed where the jet has a radius of 28.5 mm. The length at where

this radius is achieved was determined according to Equation 3.1 and was calculated to be 100 mm from HSHX inlet

$$L = TAN(11.8°) \cdot R \tag{3.1}$$

In addition, the HSHX was made of steel instead of aluminium, material that has been originally requested.

3.1.2 TEG-HS arrangement

The TEG is mechanically clamped between the HS and the HSHX. Variations within the clamping pressure can lead to variations in the TEG power generation, therefore it was decided to clamp the TEG between the HS and a plate made of aluminium. Therefore two lots of TEG+HS were made, one of them with water HS and the other with air HS.

In this section the TEG module, the heat sinks and the considerations taken into account on their clamping are described.

Experiment TEG module

A commercial TEG module from the manufacturer Alpcon A/S, shown in Figure 3.3, is used in the experiment. The module specifications are stated below.

TEG specifications at T_{hot}=623 K (350 °C) and T_{cold}=303 K (30 °C)		
Size	56×56	mm
Open circuit voltage	8.5	V
Matched load output voltage	4.3	V
Matched load output current	4.5	A
Matched load output power	$19,0$	W
Heat flow through the module	300	W
Heat flux	9.78	W/cm^2
Matched load output resistance	0.9	Ω

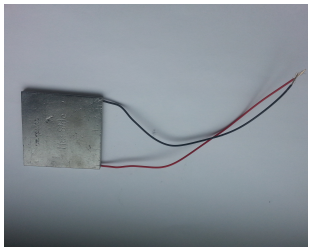

Figure 3.3: Setup TEG module.

Experiment heat sinks

The two heat sinks used in the experiment are presented. The air HS was setup with commercial components while the water HS was assembled by the AAU Energy Department staff.

The air HS consists on a anodised aluminium HS with a DC fan on its top as seen in Figure 3.4. The specifications of both the HS and the fan are held in the following tables.

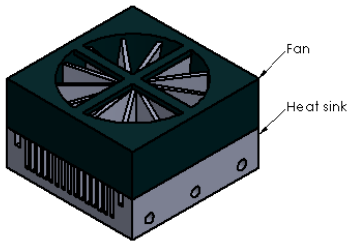

Figure 3.4: Forced air cooled heat sink with top mounted axil fan.

DC Axial Fan specifications		
Dimensions	$60 \times 60 \times 38$	mm
Power	14.4	W
Volumetric flow	107.4	m^3/h
Voltage	12	V

Air HS specifications		
Dimensions	$60 \times 60 \times 16$	mm
Nr. of fins	14	
Fin thickness	1.2	mm
Fin height	11	mm
Channel thickness	1.7	mm

The geometric characteristics of the HS are stated in the table below while it can be seen in Figure 3.5. The figure shows the HS without the lid.

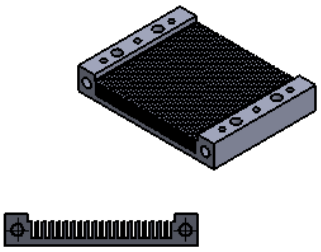

Figure 3.5: Water cooled heat sink.

Water HS specifications		
Dimensions	$60 \times 80 \times 13$	mm
Channel thickness	1.5	mm
Fin thickness	1.5	mm
Channel height	7	mm
Number of channels	19	$-$

TEG/HS clamping

The TEG clamping between the HS and the clamping plate can be seen in Figure 3.6.

The clamping is made by the action of bolts. Their specifications are: diameter of 5 mm, grade of 8.8 and withstand 580 Mpa.

A minimum pressure of 10 kg/cm^2 (980.665 kPa) is recommended by the TEG manufacturer in order to obtain an appropriate heat transfer, without thermal grease usage. While a maximum of 15 kg/cm^2 (1471 kPa) is indicated by the TEG manufacturer as the limit. This is taken in consideration in order to obtain a proper

performance and not fracture the module. The torque to be applied in the bolts is calculated according to Equation 3.2.

$$T = f \cdot F \cdot D \tag{3.2}$$

Where f is the friction factor, F is the force needed and D is the diameter. This leads to the minimum and maximum torque to be applied, held in the following table.

Clamping pressure kPa	**Torque** N/m
980	0.77
1471	1.15

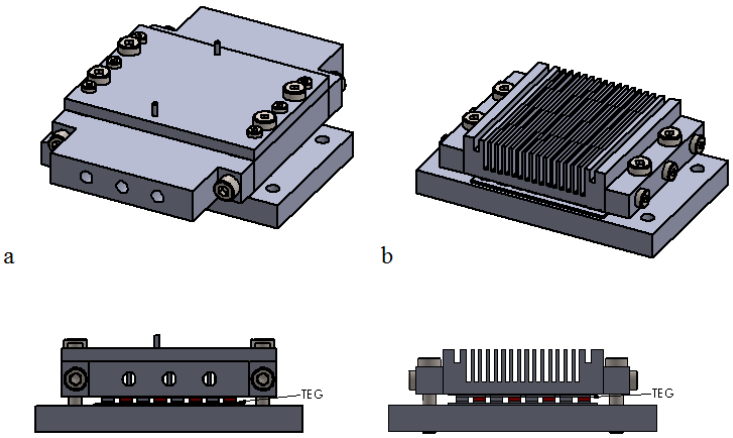

Figure 3.6: a) Water cooled heat sink / TEG module clamping b) Air cooled heat sink / TEG module clamping

3.2 Instrumentation

The hot air required for the experiment is provided by a device designed as 'Exhaust gas simulator' available in the thermoelectrics laboratory. It is basically an air heater which allows to select the temperature and volumetric flow of the air. A temperature up to 623 K (350 ° C) can be provided, while the mass flow can be varied from 23 to 120 l/min. A picture of the device can be seen in Figure 3.7.

Figure 3.7: Thermoelectrics laboratory exhaust gas simulator.

K type thermocouples were used for temperature measurement. These thermocouples have a measurement range from 473 K (200 °C) to 1523 (1250 °C) with an error of $\pm$ 0.75 %. A used thermocouple in the experiment can be seen in Figure 3.8.

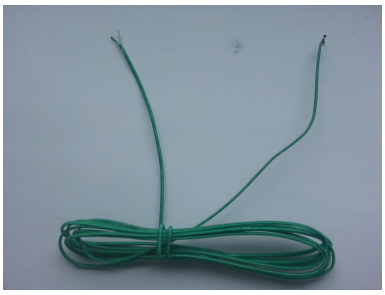

Figure 3.8: K type thermocouple.

A data acquisition unit Agilent 34970A were used to record the measurements. The TEG/fan voltage and current and temperatures. The unit is connected via USB to the laptop and allows to monitor the measurements and export the data to EXCEL files. An overview of the data acquisition system is shown in Figure 3.9.

A DC power supply TTI CPX 400SP was used to power the DC fan.

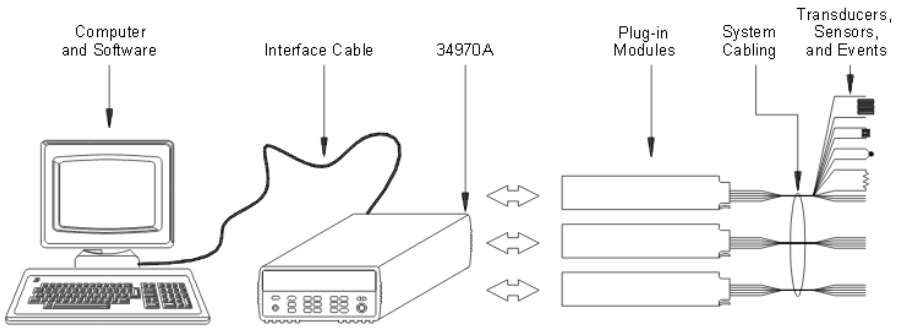

Figure 3.9: Data acquisition system overview [Agilent, 2012].

3.3 Experimental setup assembly

The designed water cooled experimental setup could not be assembled due to delays on the water HS manufacturing. In this section, the assembly of the air cooled setup described in Section 3.1 is shown.

To begin with the assembly, the HS base and the aluminium clamping plate were drilled so a thermocouple could be placed in the centre of their bases, as seen in Figure 3.10.

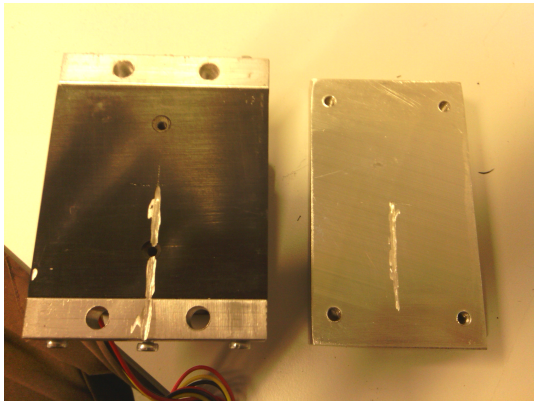

Figure 3.10: Clamping plate and HS base perforation.

Then, the TEG was clamped between the two pieces. The mechanical clamping was made by means of a torque wrench of the manufacturer Wurth. Its resolution range was from 4 to 20 $N \times m$, therefore could not be accurately know if the clamping pressure calculated in Section 3.1.2 was being applied. However it allowed us to ensure equal pressure in each of the plate corners. The air HS/TEG arrangement can be seen in Figure 3.11.

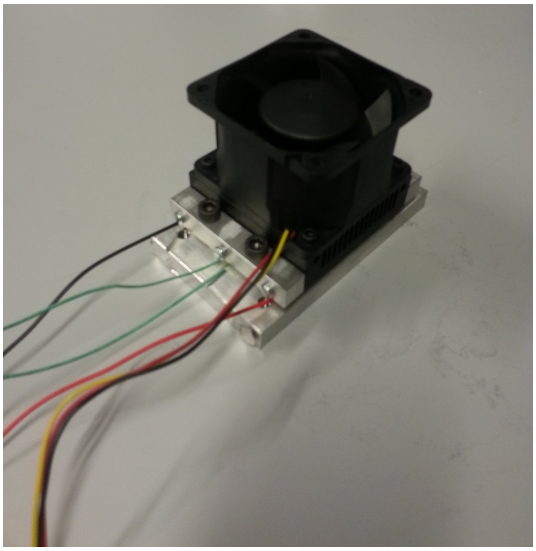

Figure 3.11: Air heat sink - TEG arrangement after mechanical clamping.

Both the exhaust gas simulator pipe and the HSHX were insulated in order to avoid heat loses. First the pieces were covered with an insulating material and covered with aluminium foil tape as seen in Figure 3.12.

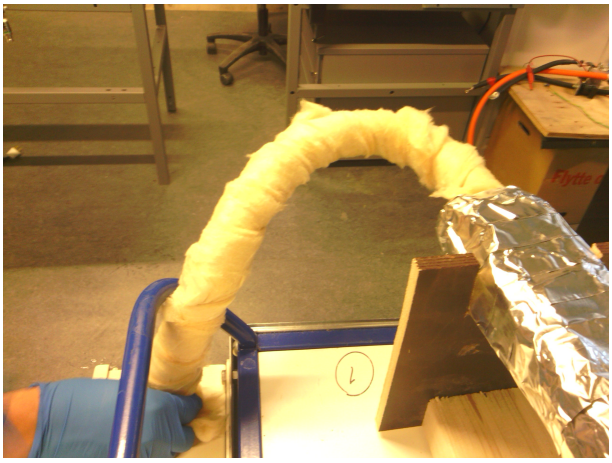

Figure 3.12: Insulation of the exhaust gas simulator tube.

In addition, small holes were drilled in the HSHX surface to place thermocouples inside it. The measuring points are labelled in Figure 3.13.

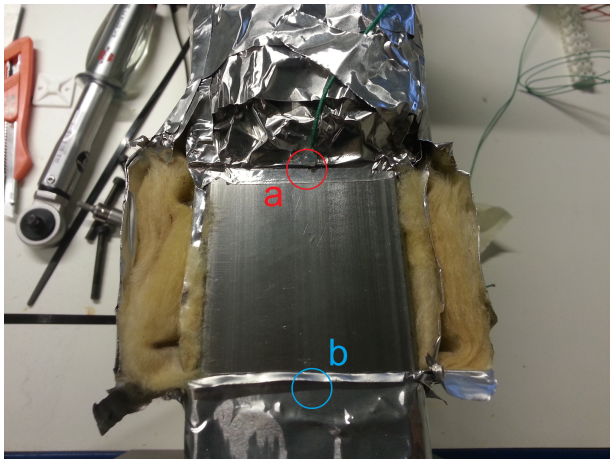

Figure 3.13: Hot air temperature measurement points: a inlet temperature. b outlet temperature.

Thermocouples were placed in the air HS as seen in Figure 3.14.

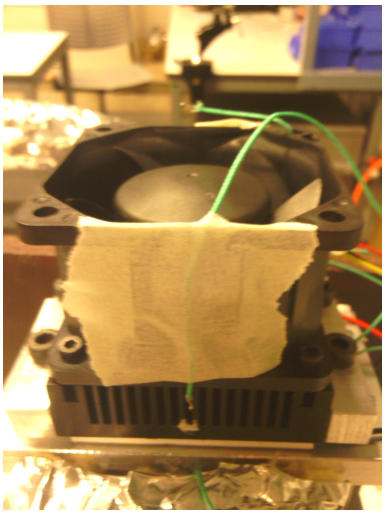

Figure 3.14: Placement of heat sink thermocouples.

To determine the TEG power production and the DC fan power consumption, voltage and current has to be measured. The voltmeter is connected in parallel between the load/fan terminals, while the amp-meter is connected in series, as seen in Figure 3.15.

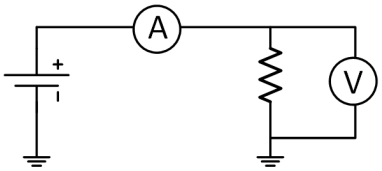

Figure 3.15: Voltage and current measurement diagram

An overview of the air cooled experimental setup is shown in Figure 3.16.

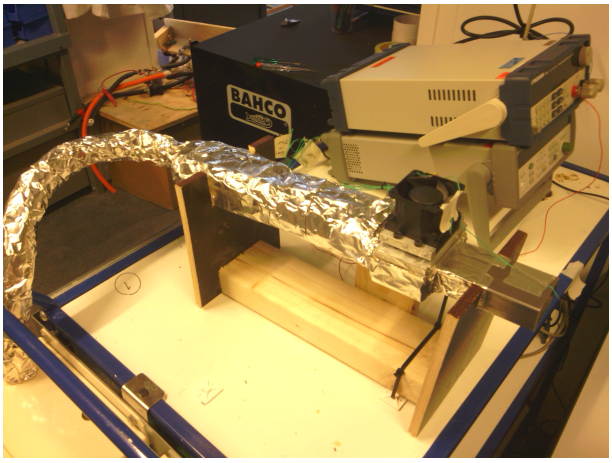

Figure 3.16: Experimental air cooled setup after insulation.

3.4 Experimental procedure

The experiment proceeded in two steps:

- First, the TEG was place at 300 mm from the HSHX inlet. Hot air was circulated through the HSHX. The TEG module was kept in open circuit. The inlet temperature of the air was fixed to 473 K (200 °C) at point **a** in Figure 3.13. The outlet temperature of the air at point **b** was measured. T_{hot}, T_{cold} and cooling air temperatures were measured. Measurements were taken with the data acquisition unit during two minutes with a sampling time of 5 seconds.

  The flow was varied from 50 to 107 l/min. The voltage of the DC fan was kept at its rated voltage: 12 V. The experiment set values are held in the following table.

Experiment 1
T_{air}**=473 K ,** V_{fan}**=12V**
$\dot{q}_{air}$ l/min
50
67
83
100
107

Measurements were taken once the TEG hot and cold side temperature were constant, for each hot air flow value.

Then, the temperature of the air inlet was fixed to 473 K (200 °C) and its volumetric flow to 100 l/min. The DC fan voltage was varied from 8 to 14 V.

Experiment 2
T_{air}**=473 K,**$\dot{q}_{air}$**=100 l/min**
V_{fan} (V)
8
10
12
14

- Second, the TEG module was placed at 50 mm of the HSHX inlet. The air inlet temperature was fixed to 563 K (290 °C) and its volumetric flow to 100 l/min. The electric load was varied from 0 to 2.2 Ω. Temperatures within the WHRS, load voltage and current values were measured.

Experiment 3
T_{air}**=563 K,**$\dot{q}_{air}$**=100 l/min**
R_{load} (Ω)
0
1
2.2

3.5 Experimental data and model comparison

The mean values of the measurements were obtained out of the experimental data.

In the following table, the mean values of Experiment 1 measurements are shown.

$\dot{q}$	$T_{gas,in}$	$T_{gas,out}$	T_{hot}	T_{cold}	$T_{air,in}$	$T_{air,out}$
50	199.25	176.48	47.61	36.78	27.18	28.46
67	199	178.81	49.53	37.55	26.86	28.32
83	199.84	181.85	51.79	38.64	27.33	28.52
100	199.98	183.69	53.33	39.27	27.23	28.51
107	199.45	184.4	54.4	39.79	28	29.12

This data was used to determine the validity of the heat exchanger model described in Chapter 2. The temperature values of the gas inlet and outlet and its volumetric flow allows to calculate the amount of heat extracted from it according to Equation 3.3.

$$\dot{Q}_{hot} = \frac{T_{eg,in} - T_{eg_out}}{\dot{q} \cdot \rho \cdot c_p} \tag{3.3}$$

The density value used in the calculation is 0.61, which is the air density at 473 K and atmospheric pressure. Then, the calculated $\dot{Q}_{hot}$ and the measured temperature difference between the gas and the TEG hot side are used to calculate the thermal resistance of the HSHX according to Equation 2.8. The estimation of the HSHX thermal resistance from the experimental data and its calculation from the analytical model for the given experimental HSHX geometry, air flow and temperature are shown in Figure 3.17.

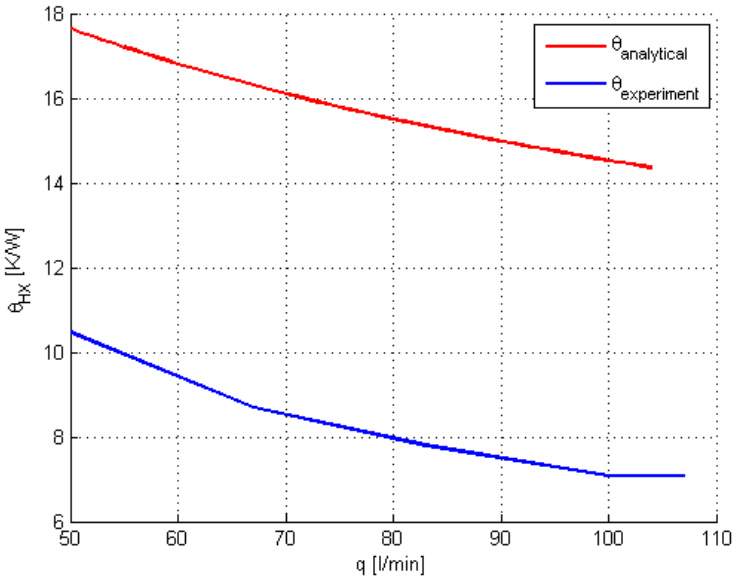

Figure 3.17: Hot side heat exchanger thermal resistance as a function of the hot air volumetric flow.

As can be seen, the calculations of the analytical model show higher heat exchanger thermal resistance prediction. The difference between them may be due to conduction heat loss through the clamping screws, error in the temperature measurement instrumentation or variations within literature material thermal conductivities and real material properties. However, the two curves follow the same tendency and therefore the model is considered valid.

The table below holds the mean values of the Experiment 2 measurements. This data was used to validate the air cooled HS analytical model.

V_{fan}	I_{fan}	$T_{gas,in}$	$T_{gas,out}$	T_{hot}	T_{cold}	$T_{air,in}$	$T_{air,out}$
8	0.66	199.92	183.78	56.3	42.04	27.55	29.31
10	0.82	199.38	183.02	54.3	40.04	27.35	28.48
12	0.94	199.98	183.69	53.33	39.27	27.23	28.51
14	1.14	198.97	182.61	52.73	38.96	27.81	29

The calculation of the HS thermal resistance out of the measured data was made as in Experiment 1.

Since the volumetric flow provided by the fan as a function of the DC voltage had been previously measured in the experiment shown in Appendix A, this values were introduced in the analytical model to calculate the HS thermal resistance. Both an

estimated value out of the experiment data and the analytical values are shown in Figure 3.18

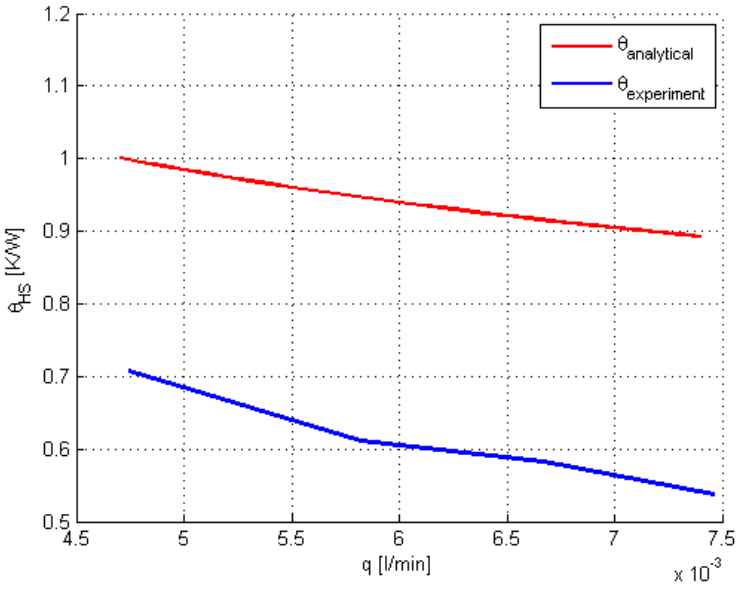

Figure 3.18: Air cooled heat sink as a function of the air volumetric flow.

The same behaviour is observed as in the HSHX case, the experimental result curve follows the analytical model trend with some displacement. Therefore the HS analytical model is considered valid as well.

On the other hand, the DC fan showed much higher power consumption values than those predicted by the analytical model, as seen in Figure 3.19.

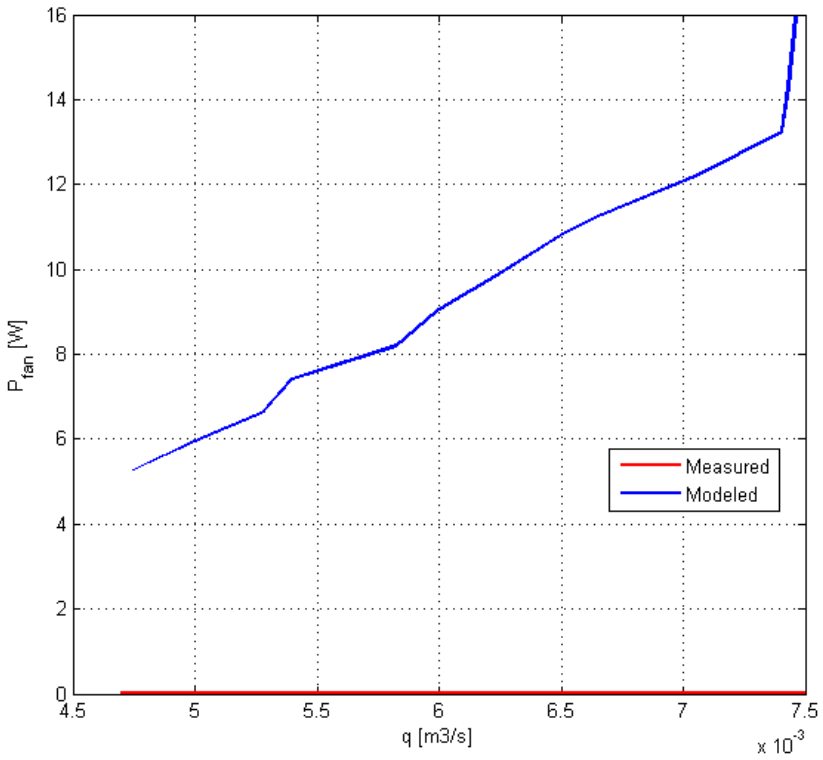

Figure 3.19: DC fan power consumption as a function of the air volumetric flow.

The equation used to predict the fan consumption in Chapter 3.5 is suitable for a compressor, however it is not adequate for a fan since it is behaviour is more complex. The volumetric flow provided by a fan depends on the pressure loss of the system (heat sink) where it is mounted on, which actually depends on the velocity of the air. A DC fan has a characteristic curve for different voltage which represents the static pressure as a function of the volumetric flow. The point where the system pressure curve crosses with the fan curve is the operation point. This is illustrated in Figure 3.20.

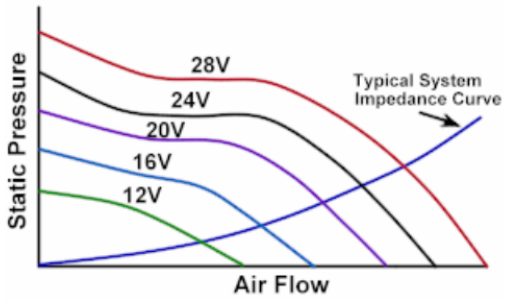

Figure 3.20: DC fan characteristic curve [Rotron, 2015].

Finally the mean values of Experiment 3 measurements are shown in the table below.

Load	V_{load}	$T_{gas,in}$	$T_{gas,out}$	T_{hot}	T_{cold}	$T_{air,in}$	$T_{air,out}$	**Current**
0	1.66	290.35	275.84	109.56	62.21	34.3	25.31	0
1	0.89	289.42	274.68	105.60	63.08	34.6	25.6	0.74
2.2	1.29	289.75	275.26	107.91	62.86	34.84	25.63	0.41

The confidentiality within the manufacturing of the TEG used in the experiment made a direct validation of Equation 2.11 and 2.12, core of the WHRS model, not possible. Therefore literature TEG data was used in the analytical model to observe the behaviour of the temperatures at the TEG hot and cold side. Figure 3.21 shows T_{hot} and T_{cold} as a function of the ratio between the load value and the TEG internal resistance.

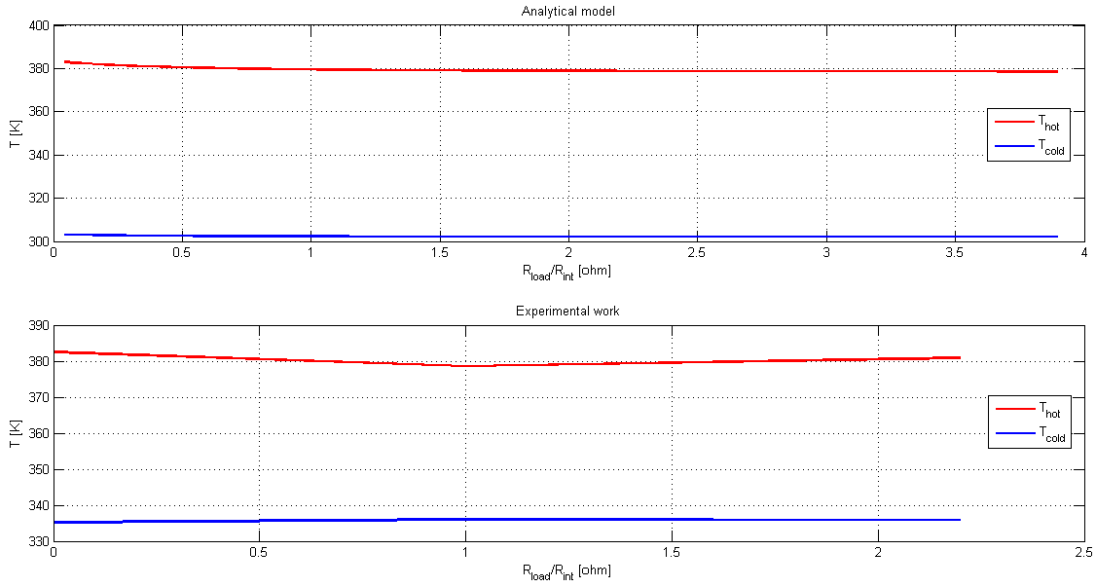

Figure 3.21: TEG hot and cold side temperature as a function of the ratio between the load and its internal resistance.

Different behaviour is observed in the model compared to the experimental results. In the analytical model, both the hot and cold side temperature show a constant decrease. The higher the ratio, the lower both temperatures. On the contrary, a cold side temperature increase is observed in the experimental work. In addition, the hot side temperature decreases. However it finds its maximum decrease when the electric load is matched with the TEG internal resistance. The experimental results look consistent. The temperature in the hot side initially decreases since heat is being transformed to electrical power. The first load value (1 Ω) is close to the TEG internal resistance value (0.97 Ω). For the second load value, less net electrical power is being produced and makes sense that T_{hot} increase since more heat is being produced due to Joule effect, compared to the previous load value. The increase of the TEG cold side temperature may be produced due to Joule effect as well. Should be remarked that the generated voltage is low, and therefore the power is low. Higher production of energy may lead to different observations.

Therefore Equation 2.11 and 2.12 cannot be considered valid according to the experimental results.

Chapter 4

Computational fluid dynamics

Computational Fluid Dynamics (CFD) is a modelling technique that uses methods and algorithms to solve and analyse problems involving fluid flows.

CFD models are based on a three dimensional solution of the fundamental conservation laws. The studied volume is divided into a multitude of sub volumes by meshing. The basic laws of mass, momentum and energy conservation are applied to each sub volume. Navier-Stokes equations, which are the fundamental basis of any CFD problem, are used to solve them [Veersteeg, H.K , Malalasekera, 2007].

The WHRS is simulated in CFD software. A CFD simulation can be divided in three steps: pre-process, process and post-process. In the flow chart in Figure 4.1, the steps to be followed to run a CFD simulations are stated. In the following sections, each of these steps to simulate the WHRS are described.

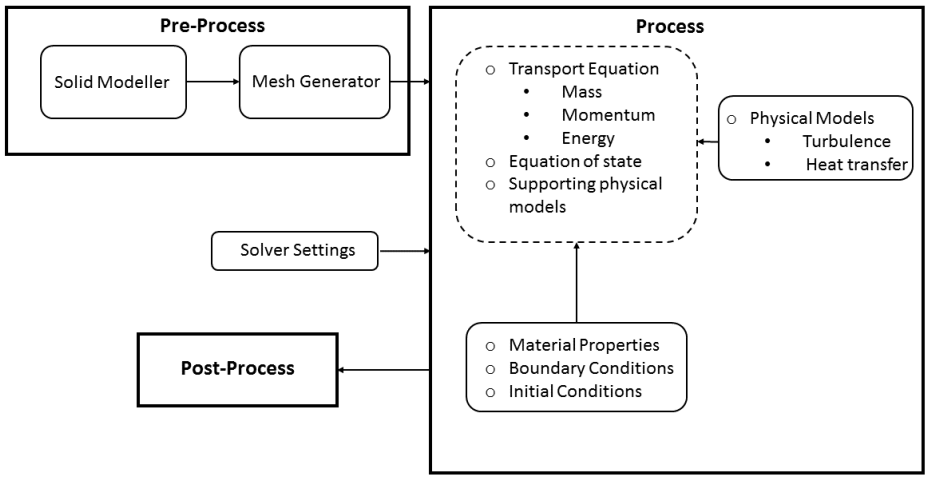

Figure 4.1: Overview of the CFD simulation.

4.1 Pre-Process

A pre-processor is used to define the computational domain of the geometry. Then the geometry is divided in control volumes by meshing.

4.1.1 Solid modelling

SolidWorks and DesignModeler were used to develop a simplified geometry of the experimental setup. The geometry was simplified by removing holes, bolts and other mechanical elements used to attach the WHRS elements. The TEG geometry was defined according to literature data [Bitschi, 2009], since the TEG module used in the experimental setup had unknown geometry. The developed geometry, for both air and water cooled WHRS, can be seen in Figure 4.2.

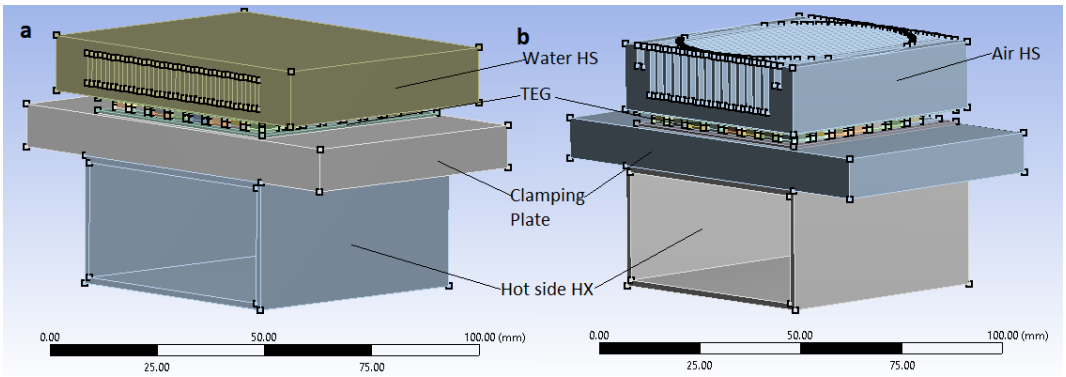

Figure 4.2: a) Simplified geometry of the water cooled waste heat recovery system. b) Simplified geometry of the air cooled waste heat recovery system.

4.1.2 Mesh generation

The computational domain, or mesh, was generated in Ansys Mesh 15. Generally, the finer the mesh, the more accurate the solution. However the fineness of the mesh also determines the computational efficiency and calculation time.

The generate mesh consists on both tetrahedron and hexahedron cells. The hexahedron cell provides a more structured mesh that can be easily controlled, leading to better mesh quality. However the tetrahedron cell is easier to implement.

The TEG module was meshed using hexahedron cells due to its simple geometry, however in the heat exchangers the use of this cell was more complicated and therefore the tetrahedron cell was used .

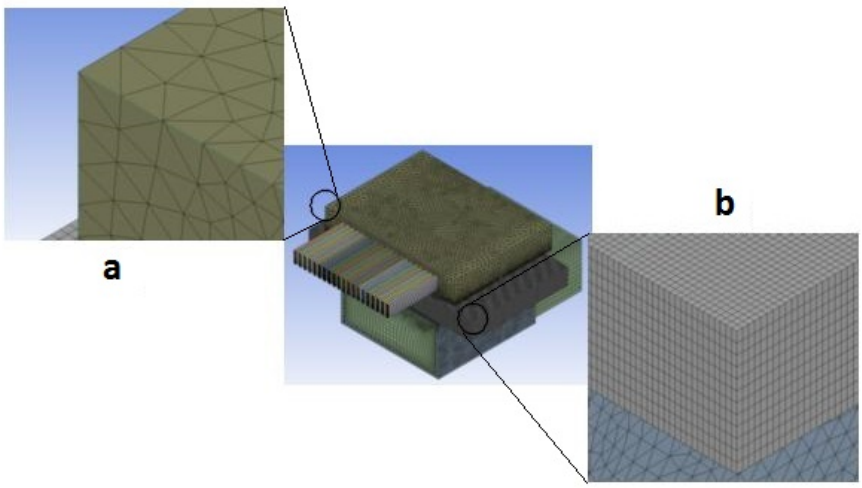

Figure 4.3: a) Tetrahedron cells b) Hexahedron cell in the water cooled waste heat recovery system geometry.

Mesh quality

The quality of the mesh plays a significant role in the accuracy and stability of the numerical computation, regardless to the type of mesh used in the domain. Important indicators of mesh quality are the orthogonal quality, aspect ratio and skewness.

- **Orthogonal quality.** In order to determine the orthogonal quality of a given cell, the following quantities are calculated for each face of the cell [ANSYS®, 2014a]:
  - the normalized dot product of the area vector of a face ($\overrightarrow{A_i}$) and a vector from the centroid of the cell to the centroid of that face ($\overrightarrow{f_i}$):

$$\frac{\overrightarrow{A_i} \cdot \overrightarrow{f_i}}{|\overrightarrow{A_i}| \cdot |\overrightarrow{f_i}|} \tag{4.1}$$

  - the normalized dot product of the area vector of a face ($\overrightarrow{A_i}$) and a vector from the centroid of the cell to the centroid of the adjacent cell that shares that surface ($\overrightarrow{c_i}$):

$$\frac{\overrightarrow{A_i} \cdot \overrightarrow{c_i}}{|\overrightarrow{A_i}| \cdot |\overrightarrow{c_i}|} \tag{4.2}$$

The minimum value from equation 4.1 and 4.2 for all the faces is then defined as the orthogonal quality. The worst cells will have orthogonal quality of 0 and the best orthogonal quality closer to 1. The minimum orthogonal quality for all types of cells should be more than 0.01, with an average value that is significantly higher [ANSYS®, 2014a].

- **Aspect ratio** is a measurement of the cell stretching. Generally, it is recommended to avoid sudden and large changes in cell aspect ratios in areas where the flow field exhibit large changes or strong gradient [ANSYS®, 2014a].

- **Skewness** is defined as the difference between the shape of the cell and the shape of an equilateral cell of equivalent volume. Highly skewed cells can decrease accuracy and destabilize the solution. For example, optimal quadrilateral meshes will have vertex angles close to 90 degrees, while triangular meshes should preferably have angles of close to 60 degrees and have all angles less than 90 degrees. As a general rule, the maximum skewness for a triangular/tetrahedral mesh in most flows should be kept below 0.95. Values above 0.95 may lead to convergence difficulties and thus require relaxing solver parameters [ANSYS®, 2014a]. The skewness average value is significantly lower.

4.2 Process

The solver makes the calculations using a numerical solution technique, based on finite difference, finite element or spectral methods. Most CFD codes use finite volumes, which is a special finite difference method. First the fluid flow equations are integrated over the control volumes, resulting in the exact conservation of relevant properties for each finite volume. Then these integral equations are discretisized, producing algebraic equations. Finally an iterative method is used to solve the algebraic equations. FLUENT software was used for solving the simulation in this project

In this section the CFD process is explained. The governing equations, physical models, boundary conditions and material properties used in the simulations are presented.

4.2.1 CFD governing Equations

The temperature and flow values are obtained by solving a set of equations formed by the continuity, momentum and energy equation with respect to computational fluid and solid domains. Within the fluid domains the equation of mass, momentum and energy conservation (Eqs 4.3-4.5) are solved to model the fluid flow, heat and mass transfer[ANSYS®, 2014b].

$$\frac{\partial}{\partial t}(\rho) + \nabla(\rho u) = S_M \tag{4.3}$$

$$\frac{\partial}{\partial t}(\rho u) + \nabla(\rho u u) = -\nabla p + \nabla \tau + S_M \tag{4.4}$$

$$\frac{\partial}{\partial t}(\rho E) + \nabla(\vec{u}(\rho E p)) = \nabla((\lambda_{eff}\nabla T - \sum_j h_j \vec{J_j} + (\vec{\vec{\tau}}_{eff} \cdot \vec{u})) + S_E \tag{4.5}$$

Where S stands by source term, τ is the viscous stress and J is the diffusion flux of species $\vec{j}$ term.

Since steady state simulations were carried out, the time dependent factor in Equation 4.3, 4.4 and 4.5 was taken out.

$$\nabla(\rho u) = S_M \tag{4.6}$$

$$\nabla(\rho u u) = -\nabla p + \nabla \tau + S_M \tag{4.7}$$

$$\nabla(\vec{v}(\rho E p)) = \nabla(\lambda_{eff}\nabla T - \sum_j h_j \vec{J_j} + (\vec{\vec{\tau}}_{eff} \cdot \vec{v})) + S_E \tag{4.8}$$

The described equations were discretized and solved using the finite volume method, implemented in a CFD code on FLUENT 15.

4.2.2 Physical models

Turbulence model

For turbulent flow, a model to represent the turbulence has to be introduced. In this project, k-ω turbulent model is used since it performs better close to walls in boundary layer flows [Casey and Wintergerste, 2000]. Thus is suitable for modelling the heat sink.

The $k-\omega$ turbulence is a two-equation turbulence model based on the transport equation for the kinetic (k) and its dissipation rate (ω) obtained from the following equations 4.9-4.10 [ANSYS®, 2014b].

$$\frac{\partial}{\partial t}(\rho k) + \frac{\partial}{\partial x_i}(\rho k u_i) = \frac{\partial}{\partial x_j}(\Gamma_k \frac{\partial k}{\partial x_j}) + G_k - Y_k - S_k \tag{4.9}$$

and

$$\frac{\partial}{\partial t}(\rho \omega) + \frac{\partial}{\partial x_i}(\rho \omega u_i) = \frac{\partial}{\partial x_j}(\Gamma_\omega \frac{\partial \omega}{\partial x_j}) + G_\omega - Y_\omega - S_\omega \tag{4.10}$$

In these equations, G_k represents the generation of turbulence kinetic energy due to mean velocity gradients. G_ω represents the generation of ω . Γ_k and Γ_ω represent the effective diffusivity of k and ω , respectively. Y_k and Y_ω represent the dissipation of k and ω due to turbulence. S_k and S_ω are source terms. These coefficients are explained in detailed in Appendix B.

Heat transfer model

The steady state energy equation, stated in Equation 4.8, is used to model the heat transfer.

The energy E of the fluid is calculated according to Equation 4.11

$$E = h - \frac{p}{\rho} + \frac{v^2}{2} \tag{4.11}$$

Where the enthalpy h is for incompressible flows is computed according to Equation 4.12, where Y_j is the mass fraction of species j and h_j is stated in Equation 4.13.

$$h = \sum_j Y_j h_j \tag{4.12}$$

$$h_j = \int_{T_{ref}}^{T} c_{pj} \mathrm{d}T \tag{4.13}$$

Finally, the viscous heating term can be neglected if the Brinkman number (Br) is much smaller than 1 ($Br \ll 1$). The Brinkman number in the simulations is between $1{\cdot}10^{-5}$ and $23{\cdot}10^{-5}$.

$$Br = \frac{\mu u^2}{\lambda \Delta T_{system}} \tag{4.14}$$

In addition, the energy equation for a solid can be simplified according to Equation 4.15

$$\nabla(\lambda_{eff} \nabla T) + S_h = 0 \tag{4.15}$$

4.3 Simulation boundary conditions

The heat transfer in the WHRS is simulated in FLUENT CFD software. In this section the set simulation boundary conditions are explained.

4.3.1 Thermodynamic properties

The WHRS materials are: Aluminium for the heat sinks and compression plate and steel for the hot side heat exchanger. The TEG module is assumed to be formed by ceramic plates made of Alumina-96, copper connection tabs and bismuth-telluride pellets. The thermal properties of this materials are listed in the table below.

Material	**Density**	**Specific heat**	**Thermal conductivity**
Bismuth-telluride*	7700	$108.06 + 0.0553T$***	0.97
Alumina-96**	3800	880	24.7
Copper	8978	381	387.6
Aluminium	2719	871	202.4
Steel	8030	502.48	16.27

Reference: FLUENT database *[Bitschi, 2009] **[Ceramics, 2015] *** in $J/mol \cdot K$

The used thermodynamic properties for the fluids used in the simulation can be seen in table below.

Fluid	**Density**	**Specific heat**	**Thermal conductivity**	**Viscosity**
Water-liquid	998.2	4182	0.6	1.003E-03
Air	1.2225	1006.43	0.0242	1.79E-05

4.3.2 Simulations boundary conditions

In this section the simulated working conditions for the WHRS are shown. Simulation 1 and 2 were developed for the water cooled WHRS. In simulation 1, the inlet velocity of the exhaust gas at the HSHX is varied, while its inlet temperature is kept constant. The cooling water boundary conditions are kept constant as well.

In simulation 2, the inlet conditions of the exhaust gas are kept constant. The inlet temperature of the cooling water is kept constant while its inlet velocity varies. In simulation 3 and 4, simulation 1 and 2 were reproduced with air as cooling fluid. The procedure of the simulations can be seen in the following table.

Simulation 1	**Simulation 2**
T_{gas}=473 K , u_{water}=0.4 m/s T_{water}=283 K, u_{gas}r. m/s	T_{gas}=473 k, u_{gas}=100. m/s T_{water}=283 K, u_{water}=. m/s
0.54	0.4
0.81	1
1.08	1.6
Simulation 3	**Simulation 4**
T_{gas}=473 K,$\dot{u}_{gas}$=1.08.m/s T_{air}=300 K, u_{air} m/s	T_{gas}=473 K,u_{gas}=1.08. m/s T_{air}=300 K, u_{air}. m/s
3.3	0.54
4	0.81
4.3	1.08
5	

Exhaust gas boundary conditions

The exhaust gas inlet conditions were a fixed temperature of 473 K and a variable exhaust gas velocity. The velocity values were set to 50, 75 and 100 l/min. For the experimental HSHX geometry, the fluid velocity is 0.54, 0.81 and 1.11 m/, respectively. The flow regime was assumed laminar. The Reynolds number of the fluid was calculated, according to Equation 2.19, in order to take this assumption. The fluid Reynolds number as a function of its velocity is shown in Figure 4.4.

The pressure loss along the HSHX had to be stated as well. It was calculated according to Equation 2.36. The pressure loss as a function of the exhaust gas velocity can be seen in Figure 4.5. As seen in the figure, the pressure loss is very low and thus constant pressure was assumed.

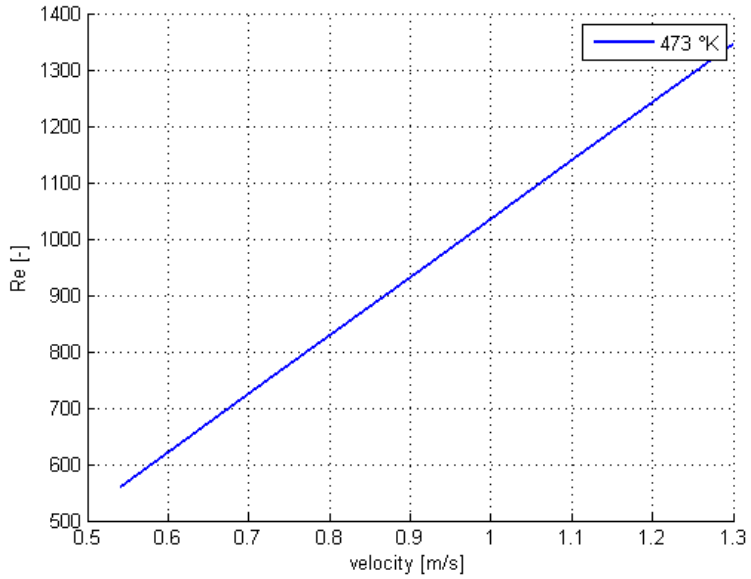

Figure 4.4: Exhaust gas Reynols number as a function of the velocity

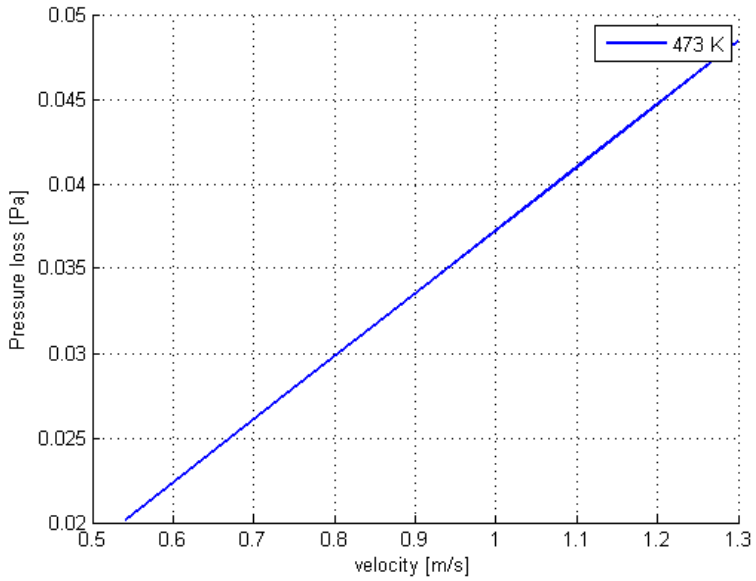

Figure 4.5: Exhaust gas pressure loss as a function of its velocity

Cooling water boundary conditions

In the water cooled WHRS simulation, the cooling water flow regime was considered both laminar and turbulent. The water velocity at the HS inlet were selected in order to obtain both flow regimes. The Reynolds number of the water can be seen as a function of its velocity in Figure 4.6. The velocity was fixed to 0.4, 1 and 1.6 m/s. Its inlet temperature was fixed to 283 K.

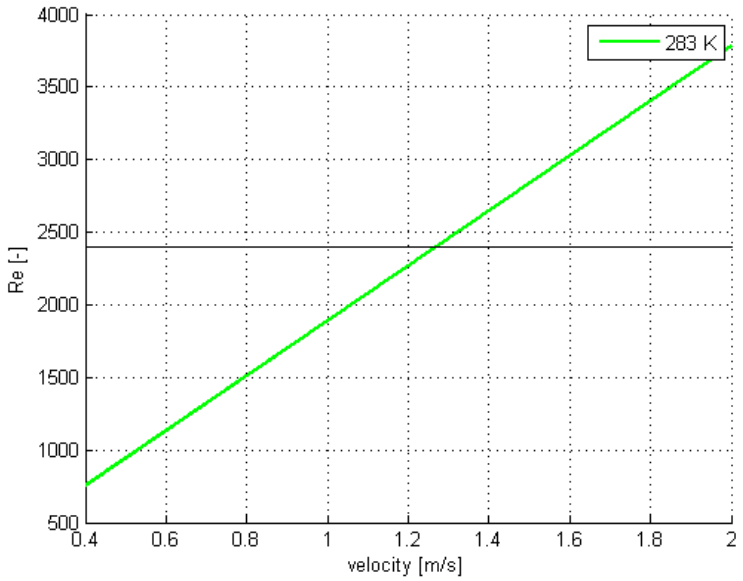

Figure 4.6: Reynolds nr in water heat sink channel as a function of the velocity for different temperatures

The pressure loss in each HS channel was introduced. It was calculated according to Equation 2.36. The pressure loss as a function of the water velocity can be seen in Figure 4.7.

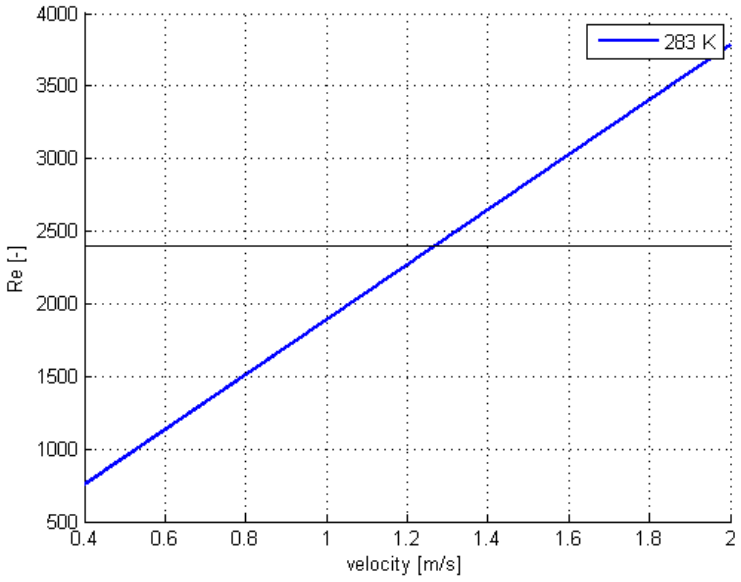

Figure 4.7: Pressure loss in the water HS at different temperatures

Cooling air boundary conditions

The cooling air temperature was set to 300 K. The cooling air flow regime in the HS channel was considered laminar, for the given inlet velocities. The set velocities are 3.3, 4, 4.6 and 5.2 m/s. The cooling air Reynolds number as a function of its velocity is shown in Figure 4.8. As can be seen, laminar flow can be assumed for this velocities.

The pressure loss in each HS channel can be seen in Figure 4.9 as a function of the air velocity. The pressure loss for the set velocities is 8, 9.5, 10.4 and 12.2 Pa, respectively.

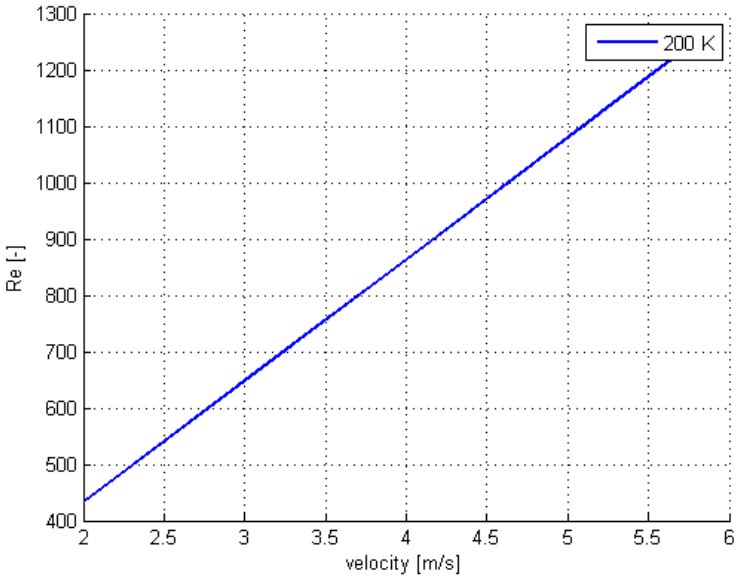

Figure 4.8: Cooling air Reynolds number as a function of its velocity.

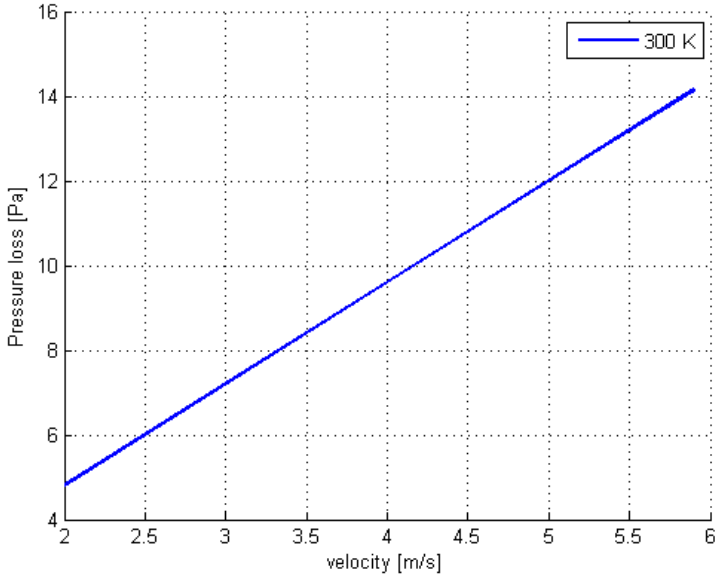

Figure 4.9: Cooling air pressure loss as a function of its velocity.

4.3.3 Mesh independence study

To determine the used amount of cells, a mesh independence study was carried out. The objective is to determine the influence of the amount of cells on the results, since it determines the convergence speed and computing accuracy. The independence study was developed for both models simulations.

Several mesh sizes were tested, varying the cell number from 750,000 to 6,200,000 globally. The influence of the cell number on the heat transfer from the exhaust gas was observed.

For the water cooled model, the variation between 1.5 million cells and 3.2 million cells showed difference around 0.5%. For the air cooled model, the variation between 4.8 million cells and 6.2 million cells showed a difference around 0.6%.

According to the study, 1.5 million cells and 4.8 millions cells are the best choice to satisfy efficiency and accuracy at the same time. Because of the computational power requirements and time limitation, a cell number of 144000 for the water simulation and 111000 for the air simulation were chosen. These limitation result in much higher residuals in the continuity equation. Therefore the heat transfer computation can not be considered valid. However the calculation time is reduced and it does not affect the accuracy of the temperatures within the WHRS. Figures 4.10 and 4.11 show the residual difference between meshes of 114 thousand and 2.4 million cells in the water simulation.

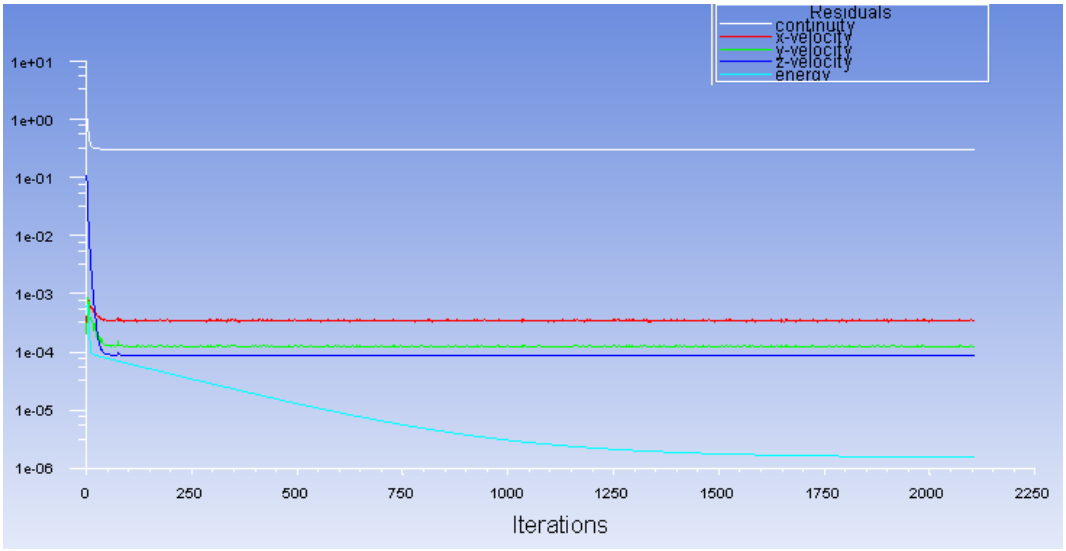

Figure 4.10: Residuals of water simulation with a 111000 cells.

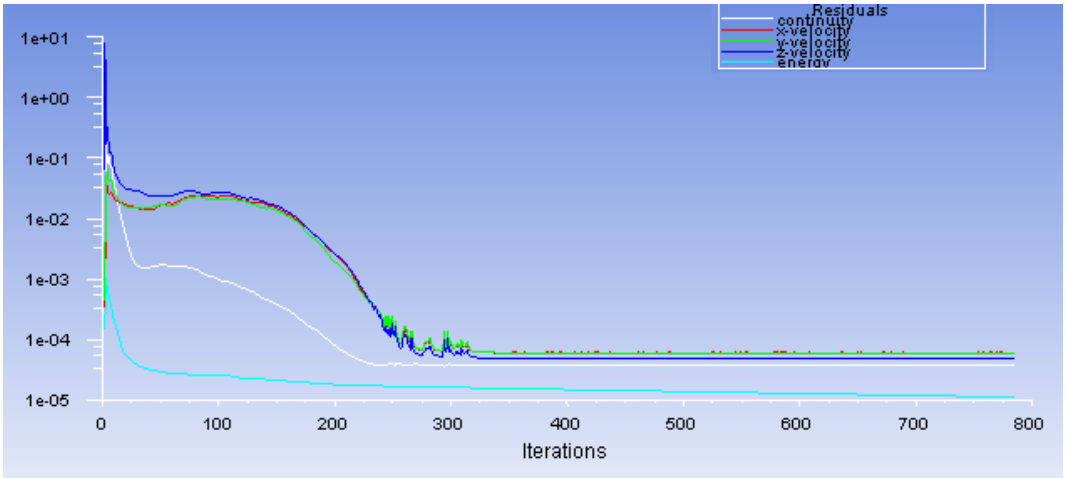

Figure 4.11: Residuals of water simulation with a 2.4 millions cells.

In Figures 4.12 and 4.13 the progression of the temperature in the simulation. These graph indicate how fast the simulations are given that 114 thousand cells simulation took 20 minutes to reach 800 iterations and 2.4 million cells took two hours to reach 800 iterations.

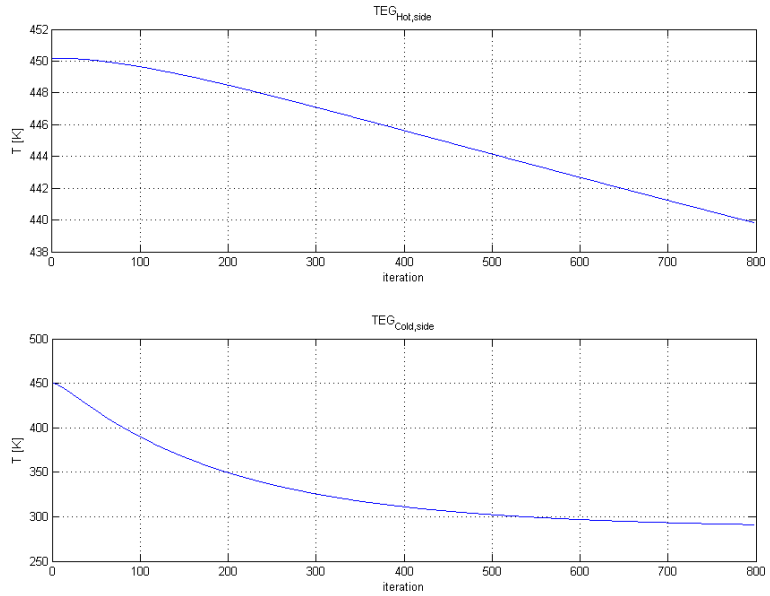

Figure 4.12: Progression of the temperature in the 114 thousand cells simulation

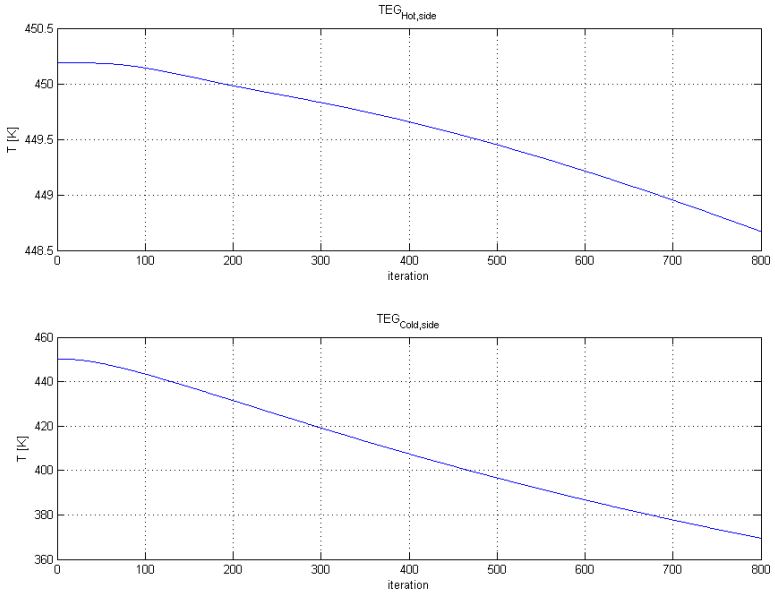

Figure 4.13: Progression of the temperature in the 2.4 million cells simulation

4.3.4 FLUENT convergence criteria

In this section the convergence criteria used in the simulations introduced before is stated.

Convergence is when an iterative process is repeated until the change of the variable from one iteration to the next is smaller than a fixed convergence criteria. Once the change is smaller than the convergence criteria, the solution can be considered converged.

The average temperature values of the TEG hot and cold side were calculated in the simulations. A convergence criteria of 10^{-4} was set in the calculation of those variables.

4.4 Result and discussion

In this section the result from the CFD simultion are shown and discussed. The simulation result of simulations 1 and 2 are presented. The solution of simulations 3 and 4 presented a divergent behaviour and therefore the results to this simulations are not presented.

Figure 4.14 shows the result of the TEG hot and cold side temperatures for the inlet conditions of simulation 1. In addition, the temperature values calculated by the analytical model for the same working conditions are shown. The TEG cold side temperature calculated by both models match, with an average temperature difference of 0.79 K.

The prediction of the hot side temperature does not show so good correlation between the CFD and the analytical model. The CFD presents a difference of 16 K between the hot side temperature calculated for a exhaust gas velocity of 5.4 m/s and the one calculated at 0.8 m/s. In addition, the CFD simulation shows a decrease in the TEG hot side temperature for exhaust gas velocity increase. This implies that the solution of the TEG hot side temperature calculation has not converged.

As shown in Figure 4.12 hot side temperature needs more iterations to converge than the cold side. The same behaviour is observed in simulation 2, as shown in Figure 4.15.

Because of the convergence problem that are shown in the result the validation of the analytical model can not be done with CFD simulation. Though the result show good correlation between them on the cold side of the TEG.

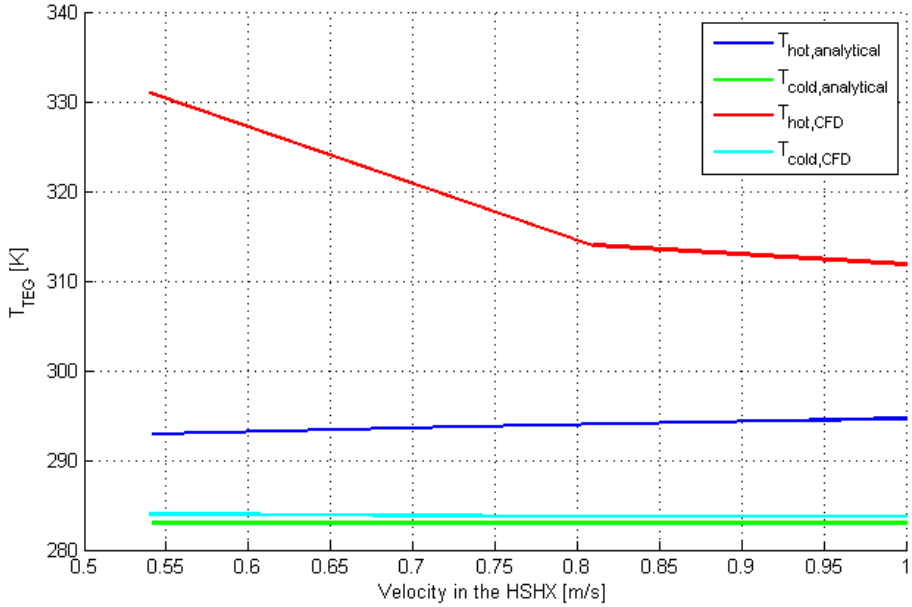

Figure 4.14: Comparison between the CFD and analytical estimation of the TEG temperatures in simulation 1.

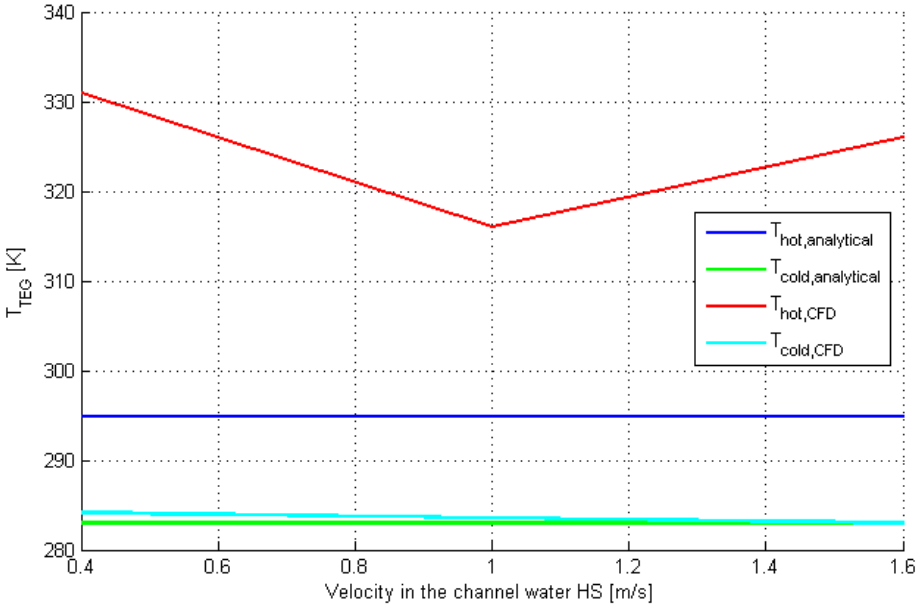

Figure 4.15: Comparison between the CFD and analytical estimation of the TEG temperatures in simulation 2.

Chapter 5

Optimization

An optimization problem consists in determining optimum values of a certain amount of design variables such that they minimize (or maximize) a specific function termed the objective function, while satisfying a set of requirements designed as constraints [Lund, 2015]. The standard formulation of an optimization problem is as follows:

Minimize: $f(x)$

Subject to $= \begin{cases} h_j(x)=0;\ \text{j=1,...,p} \\ g_i(x) \leq 0;\ \text{i=1,...,m} \end{cases}$

where x is a vector containing the design variables, $f(x)$ is the objetive function, $h_j(x)$ are p equality constraint functions and $g_i(x)$ are m inequality constraint functions. As stated above the standard form of an optimization problem is actually a minimization problem, however a maximization problem can be transformed into minimization problems by changing the sign of f [Lund, 2015].

5.1 Problem definition

In this section, the objective function and the design variables of the optimization problem are defined. In addition, the constraints within the design problem are set and explained.

The net power provided to the electric load is to be maximized, therefore the objective function to be minimized is the negative net power as stated in Equation 5.1.

$$P_{net} = -(P_{load} - P_{pump}) \tag{5.1}$$

Where P_{load} and P_{pump} were stated in Equation 2.7 and Equation 2.35 respectively. Since Equation 2.42 was found not valid to predict the power consumption of a DC fan, it was assumed that the cooling air is provided by means of a compressor.

As seen in previous sections, the section of the HSHX determines the velocity of the exhaust gas and therefore the convection heat transfer resistance. As it was seen,

a HSHX of 60 × 60 × 30 mm led to a very high thermal resistance. Therefore the optimization problem was formulated in such a way that the TEG module size varies as the HSHX surface does. The size of the TEG module has then to be matched with the size of the HSHX $a \times b$ surface. The geometry of the HSHX and the TEG module are shown in Figure 5.1, where s is the separation between pellets.

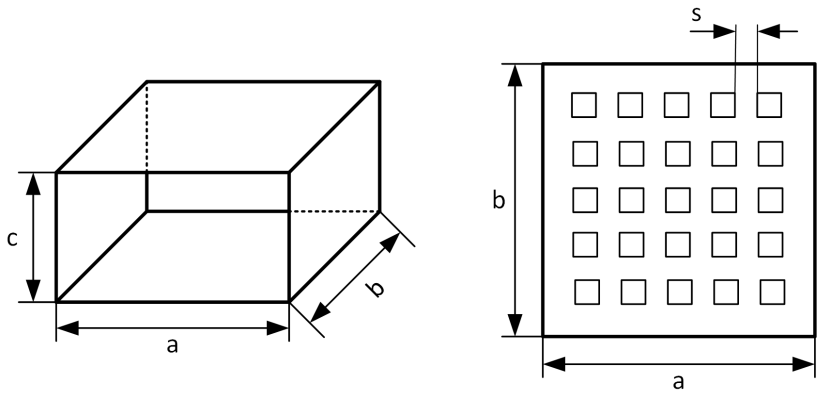

Figure 5.1: Hot side heat exchanger and TEG module geometry.

The HSHX surface and the TEG module surface are considered equal. If size the separation between the pellets and the module edges is considered equal to the separation between pellets, the two geometries can be related by means of introducing a search variable N_{rows}, which is the number of rows of thermoelectric pellets, as seen in Equation 5.2. Since a is equal to b, the number of columns is equal to the number of rows, therefore the number of legs in the optimization program can be calculated according to Equation 5.3. The third HSHX parameter c is set as a search variable too.

$$a = s + (\sqrt{A_{legs}} + s) \cdot N_{rows} \tag{5.2}$$

$$N_{legs} = N_{rows}^2 \tag{5.3}$$

The ceramic plates thermal resistance depends as well on a and b, given the conductivity of the material and plate thickness, the plate thermal resistance is computed according to Equation 2.13.

Both heat sinks optimal designs are obtained by means of setting the channel thickness, channel height, cooling fluid velocity and number of channels as search variables. The number of channels is limited by the surface $a \times b$ according to Equation 5.4.

$$N_{ch} = \frac{a - \delta_f}{\delta_{ch} + \delta_f} \tag{5.4}$$

In addition, T_{hot} and T_{cold} are also set as design variables. The temperature gradient across the TEG pellets is set as a function of the WHRS elements thermal resistances and the total temperature gradient by introducing Equation 2.11 and 2.12 as equality constraints of the optimization problem.

Finally, the thermal impedance match condition is imposed as a equality constraint according to Equation 5.5.

$$R_{TEG} = R_{HX} + 2 \cdot R_{cer} + R_{HS} \tag{5.5}$$

5.2 Optimization boundary conditions

The optimization problem is bounded with a car diesel engine exhaust gas data. The exhaust gas amount can vary depending on the engine size and how it is operated by the driver. Due to this fact, results from the US federal test procedure (FTP-75) city driving cycle are used to set the boundary conditions. Figure 5.2 shows the variation of the mass flow rate during the test, it varies from 5 g/s to 45 g/s. The mean mass flow rate , 20 g/s [Wang et al., 2013], is set to bound the problem. The temperature of the exhaust gas when leaving the vehicle catalytic converter during the test can be seen in Figure 5.3. The temperature fluctuates around a value of 500 ° C (773 K), thus the exhaust gas temperature boundary condition is set to this value.

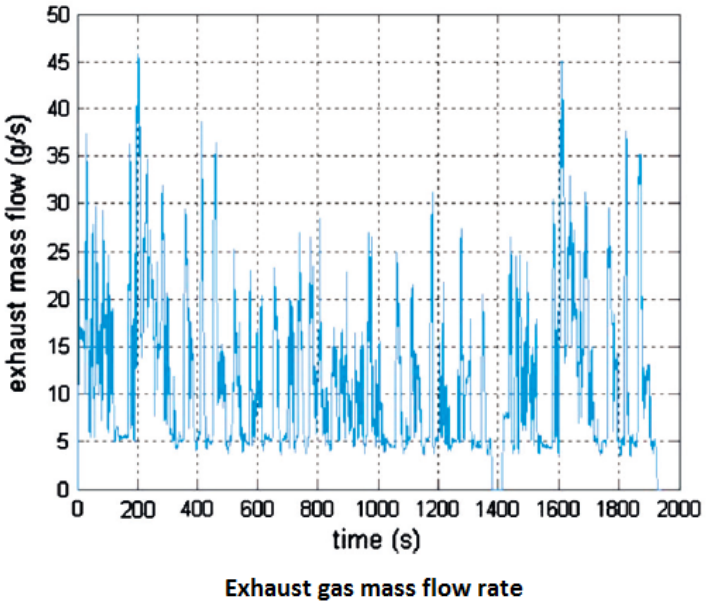

Figure 5.2: Variation of the exhaust gas mass flow rate for the FTP-75 drive cycle [Wang et al., 2013].

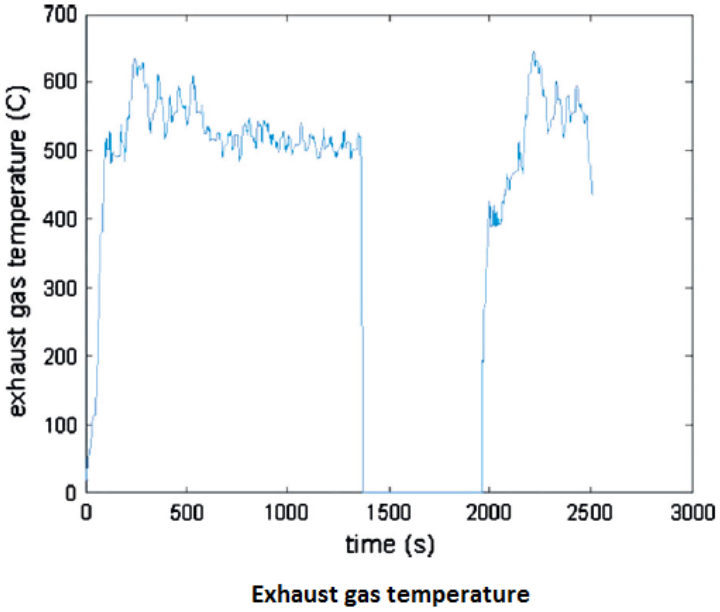

Figure 5.3: Variation of the exhaust gas temperature for the FTP-75 drive cycle [Wang et al., 2013].

The TEG material properties and pellets geometry used for the optimization problem are held in the table below [Bitschi, 2009]. The TEG was fixed to matched electric load working condition.

TEG data		
Seebeck coefficient	$\alpha_p + \alpha_n = 3.47 \cdot 10^{-4}$	V/K
Thermal conductivity	$\lambda_p = \lambda_n = 0.97$	$W/m \cdot K$
Electrical conductivity	$\sigma_p = \sigma_n = 75187.97$	$S \cdot m$
Length of the legs	1.4	mm
Area of the legs	19	mm^2
Separation between legs	2.236	mm

The electrical thermal contact parameter r was set to 0.2. The thermal contact resistance parameter n and the contact resistance thickness l_c were fixed to 0.1 and 0.7 mm, respectively [Min, 2005].

The ceramic plates used to place the pellets between are usually made of Alumina, which thermal conductivity has a value of 30 $W/m \cdot K$ [Rezania and Rosendahl, 2012]. A plate thickness of 0.2 mm is set.

The thickness of the fins was set to 1 mm while the thickness of the HS base was set to 0.5 mm. Finally the temperature of the cooling fluid was set to 283 K for the

water and to 300 K for the air.

The thermodynamic properties of the fluids are held in the following table.

Fluid	$T(K)$	ρ	λ	μ	c_p	Pr
water	283	1000	0.56	$13.12{\cdot}10^{-4}$	4188	9.69
water	293	988	0.58	$10{\cdot}10^{-4}$	4183	7.18
air	773	0.45	0.055	$35.63{\cdot}10^{-6}$	1082	0.6
air	300	1.17	0.025	$18.57{\cdot}10^{-6}$	1005	0.72

5.3 Optimization tools

Matlab includes a built-in function called *fmincon* which allows to solve optimization problems with non-linear constraints, as the problem does. Therefore it was chosen as the solver for the problem. However the problem requires that two of the search variables, N_{ch} and N_{rows}, have to be integer. Unfortunately $fmincon$ can not impose a variable to adopt integer values.

On the other hand, Matlab includes a function that actually imposes this requirement to a design variable. It is called *ga* and simulates the stochastic optimization algorithm 'genetic algorithm'. However it just accept non-linear inequality constraints, and not equalities. Since Equation 2.11 and 2.12 are crucial in this problem, it was decided to solve the problem by using *fmincon* although a slightly deviation from the optimal design is expected.

The function $fmincon$ requires the following inputs: an objective function, a function including the non-linear constraints, lower and upper bounds for the design variables, and an initial point. It returns a possible local minimum. This means that the solution provided by the function is not necessary the best optimal solution, this is illustrated in Figure 5.4. In addition, the computed optimal point may not satisfy the constraints, according to Matlab's help menu. Therefore the optimal design variables values were introduced afterwards in the constraints to determine if they were satisfied or not.

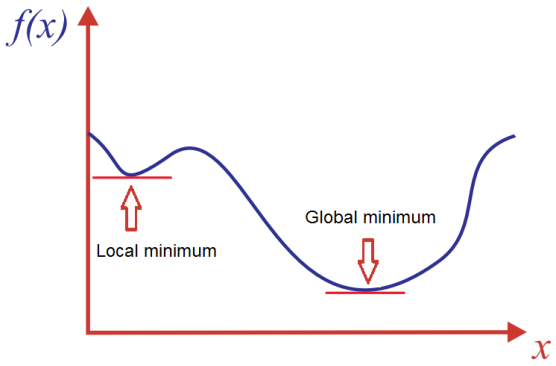

Figure 5.4: Function with local and global minimum.

Different functions were developed to predict the heat exchangers thermal resistance and pressure losses, based on the equations stated in Chapter 2. The objective function and the constraint functions made use of them in order to predict the behaviour of the HSHX and the HS for the different search variable values.

5.4 Optimization procedure

As stated in the previous section, the function used to solve the optimization problem requires lower and upper bounds for the design variables. This bounds restrict the problem. The optimization proceeded as follows:

First the lower bounds of the variables were set to 0, while the upper bounds were set to infinity. It was found that the solver looks for the optimal solution in low thickness channels solutions and low heat exchanger duct height. Therefore the optimization problem was solved for different variables boundary conditions. Most of them were kept constant, while δ_{ch} and c bounds were varied. In addition, different initial points were introduced.

In the following tables the variables boundary conditions for water and air cooled HS, respectively, are summarized.

Variable	Lower bound	Upper bound	Unit
δ_{ch}	Variable	10	mm
H_{ch}	1	5	mm
u_{fluid}	0	1	m/s
$N_{channels}$	1	30	-
N_{rows}	2	15	-
c	Variable	20	mm
T_{hot}	373	673	K
T_{cold}	283	448	K

Variable	Lower bound	Upper bound	Unit
δ_{ch}	Variable	10	mm
H_{ch}	0	20	mm
u_{fluid}	0	20	m/s
$N_{channels}$	1	40	-
N_{rows}	2	15	-
c	Variable	20	mm
T_{hot}	373	673	K
T_{cold}	300	448	K

The values used for the remaining variables (δ_{ch} and c) lower bounds are shown in the table below.

Case	δ_{ch}	c
1	1	20
2	0.5	20
3	0	20
4	1	5
5	1	10
6	1	15

The design variables values provided by *fmincon*, for the different boundary conditions, are shown below:

Water	**1**	**2**	**3**	**4**	**5**	**6**
δ_{ch}	1.7	0.5	0.2	1.8	1	1
H_{ch}	5	3.1	3.1	3.8	3.5	3.1
u_{water}	0.32	0.99	0.32	1	0.52	0.54
N_{ch}	29.92	25	27.59	28.5	26,36	18.57
N_{rows}	12.12	4.49	4.99	12.12	7.8	5.45
c	20	20	20	6.8	10	15
T_{hot}	555.23	544.17	543.36	565.27	556.27	551.02
T_{cold}	304.44	290.1	289	302.86	294.97	293.73
R_{HX}	3.23	3.07	3.06	0.40	1	2.05
R_{HS}	0.24	0.067	0.055	0.027	0.038	0.07
R_{TEG}	3.48	3.15	3.13	0.43	0.96	2.13
P_{TEG}	5.68	6.43	6.46	50.31	20.7	9.77
P_{pump}	$7.8{\cdot}10^{-5}$	0.01	0.03	0.003	0.007	0.003
P_{net}	5.68	6.43	6.47	50.3	20.7	9.77
a	30.3	31.8	31.9	82.1	53.7	38.2
Ratio (W/cm^2)	0.61	0.63	0.64	0.74	0.72	0.68

Air	**1**	**2**	**3**	**4**	**5**	**6**
δ_{ch}	1	0.8	0.8	1.5	13	1
H_{ch}	20	20	20	20	20	20
u_{air}	18.93	16.8	16.8	13.05	14.8386	19.16
N_{ch}	26.98	30.93	30.93	39.99	40	34.15
N_{rows}	7.99	8.08	8.08	15	13.82	10.17
c	20	20	20	8.5	10	15
T_{hot}	611.776	610.19	610.19	644.52	635.98	618.52
T_{cold}	352.6135	350	350	391.66	379.73	357.5
R_{HX}	1.6821	1.66	1.66	0.41	0.51	1.022
R_{HS}	0.3	0.35	0.35	0.19	0.18	0.21
R_{TEG}	1.97	1.93	1.93	0.56	0.66	1.22
P_{TEG}	21.37	22	22	71.6	62.49	35.07
P_{pump}	1.74	2.03	2.03	1.57	2.11	2.88
P_{net}	19.63	19.96	19.96	70.03	60.37	32.23
a	55	55	55	42.4	93.4	69.3
Ratio (W/cm^2)	0.65	0.65	0.65	0.68	0.69	0.67

5.5 WHRS optimal designs

The ratio between net power production and TEG surface of the optimal design candidates obtained in the previous section are checked in order to select the most suitable candidate. Case 4 was selected for the water cooled WHRS while case 5 was chosen for the air cooled WHRS.

The integer design variables are truncated and the optimal design is shown in the following table.

Fluid	δ_{ch}	H_{ch}	u_{fluid}	N_{ch}	N_{legs}	**a**	**c**
water	1.8	3.8	1	29	144	81.37	6.8
air	13	20	14.83	40	196	94.56	10

Chapter 6

Analytical model results and discussion

Once an optimal design were obtained for both water and air cooled WHRS, their performance were simulated in the analytical model for different working conditions. Since the set of equations defining the model has non-linear equations, a solver is needed. The built-in MATLAB function *fsolve* was not providing convergence on the equations set solution, therefore a non-linear equation solver based on Newton's method was used [Mendes, 2011]. A short description of the method can be found in Appendix C.

The simulation boundary conditions regarding materials and thermodynamic properties are those used in the optimization problem in Chapter 5.

6.1 Water cooled WHRS results

6.1.1 Simulation 1. Performance for variable exhaust gas mass flow

The first simulation carried out consists on predicting the performance of the water cooled WHRS for a variable exhaust gas mass flow. The amount of exhaust gas were varied from 5 to 45 g/s. Its temperature was fixed to 773 K, electrical impedance match condition was assumed and optimal cooling water velocity. In addition, two different cooling water temperatures were considered: 283 and 293 K.

The net power production was calculated, in addition the voltage and current provided to the load was calculated too.

As seen in Figure 6.1, the power provided to the load at the minimum, mean and maximum exhaust gas mass flow is 5.5, 45 and 66.4 W, respectively, for a cooling water temperature of 283 K. In addition, with a cooling water temperature of 293 K, the minimum, mean and maximum power production take place at 5.26, 43 and 63.6 W.

The slope of the graph shows an inflexion point on its trend at the mean mass flow value. The curve shows a higher slope between the minimum and mean exhaust

gas mass flow value, compared to the slope between the mean and the maximum point. This looks consistent since the WHRS was optimized to operate at the mean mass flow rate.

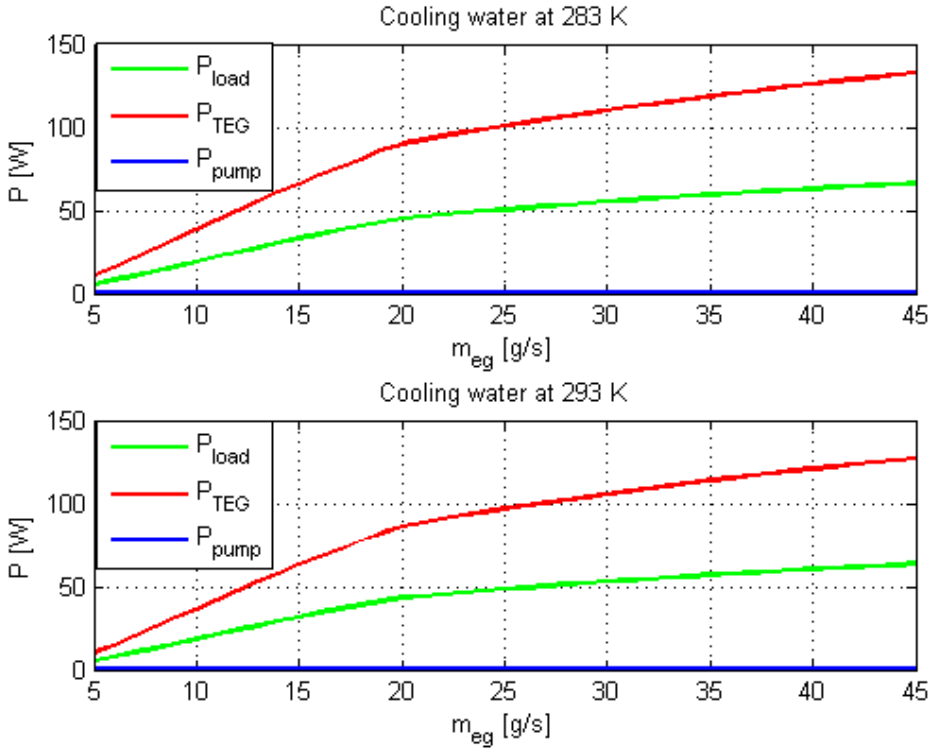

Figure 6.1: Water cooled WHRS power production as a function of the exhaust gas mass flow.

The same behaviour is observed in the voltage and current curves, as seen in Figure 6.2. The minimum, mean and maximum load voltage values are 0.91, 2.61 and 3.16 V while the current values are 6, 17.67 and 20.95 A when cooling water at 283 K is used. For cooling water at 293 K, the voltage values are 0.89, 2.55 and 3.1 V while the current values are 5.9, 17.7 and 20.52 A.

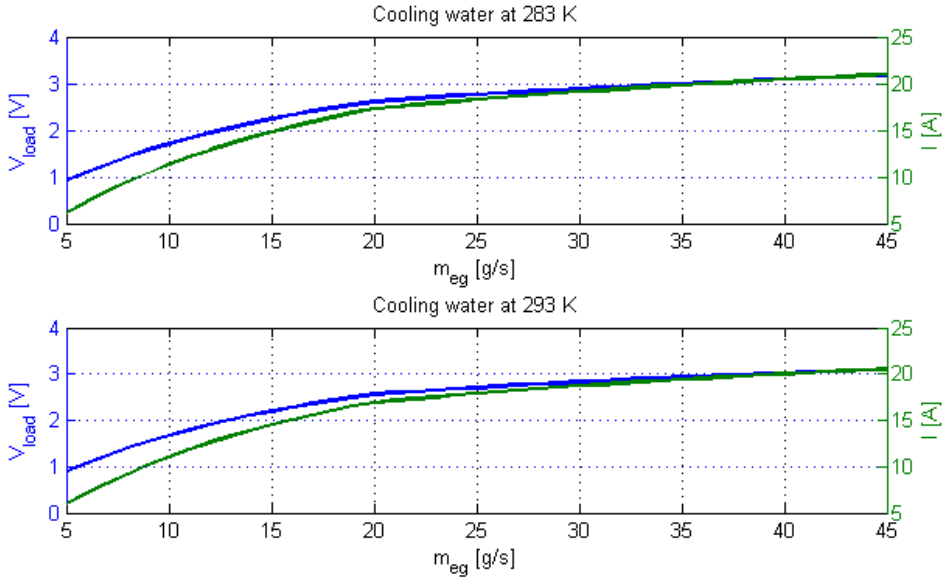

Figure 6.2: Water cooled WHRS load voltage and current as a function of the exhaust gas mass flow.

No significant additional power production is observed by using cooling water at 283 K.

6.1.2 Simulation 2. Performance for variable electric load

In the second simulation, mean exhaust gas temperature and mass flow were assumed. The value of the electric load is varied from 0 to 5 Ω. Again, the two cooling water temperatures were considered. The performance of the water cooled WHRS for different load values is shown in Figure 6.3. As can be seen, the power provided to the load finds its maximum value for a load value below 0.5 Ω, this means that the internal resistance of the TEG module is low. Therefore this really constraints the load that can be efficiently supplied by the TEG module. Once the load value of 1 Ω is surpassed, the losses due to Joule effect are much lower than the power provided to the load. However the power production has much lower values than at electrical impedance match condition. In Figure 6.4, the voltage and current production as a function of the load is shown. It can be observed that the maximum power production occurs when both curves cross. In addition, low voltage and high current is observed for low load values, while high voltage and low current is provided to the load when it has higher values.

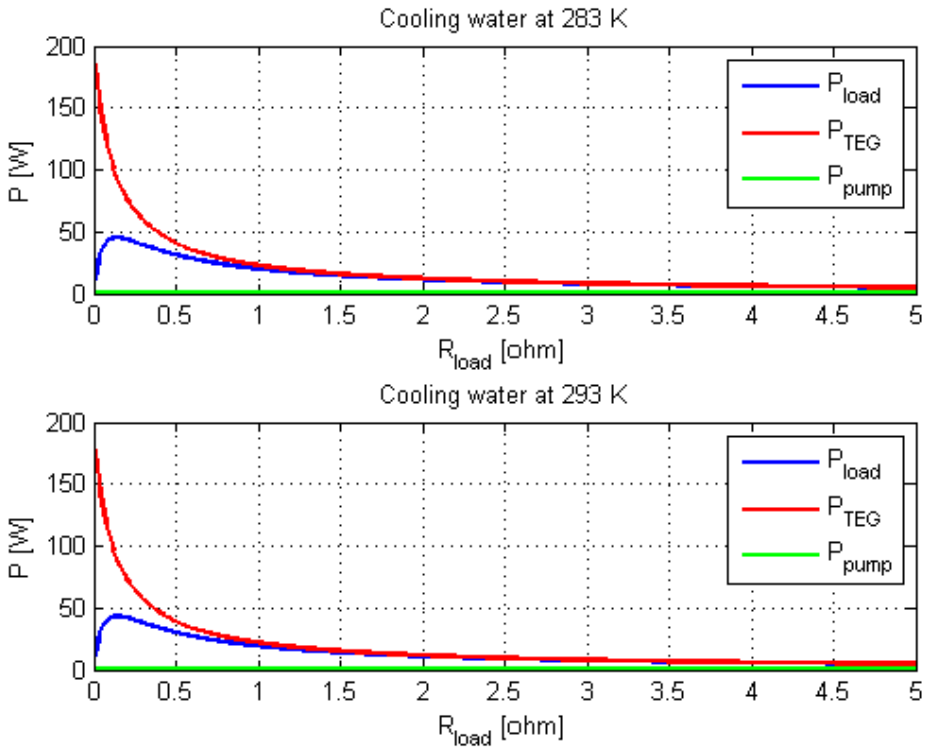

Figure 6.3: Water cooled WHRS power production as a function of the electric load.

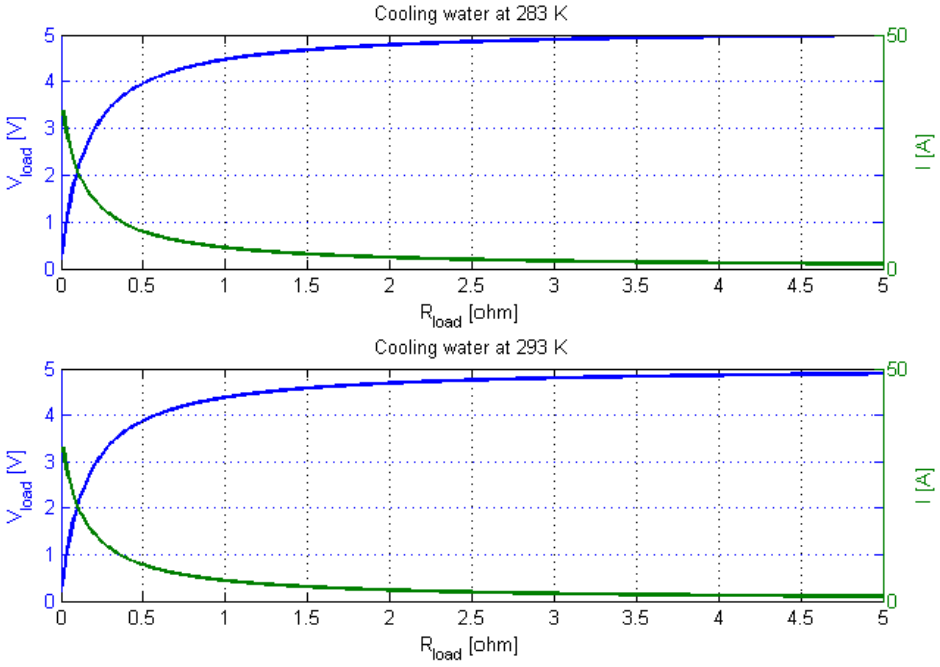

Figure 6.4: Water cooled WHRS voltage and current production as a function of the electric load.

6.1.3 Simulation 3. Performance for variable cooling water velocity

Finally, different cooling fluid velocities were considered, electrical impedance match condition is assumed and the exhaust gas temperature and mass flow values are fixed to their mean values. In Figure 6.5, the power provided to the load and the power consumed by the cooling water pump are shown as a function of the cooling fluid velocity. It can be seen that the power provided to the load does not experiment significant decrease if the cooling water velocity is decreased from the optimal design velocity. In addition, it is observed that when cooling water at 293 K is used, turbulent flow occurs when its velocity approximates to the optimal design velocity. Since cooling water at 283 K was assumed in the optimization problem, the optimization function approached the boundary between laminar and turbulent flow as optimal condition. However slight variations in the thermodynamic properties of the water for an increase of 10 K makes the flow reach turbulent flow.

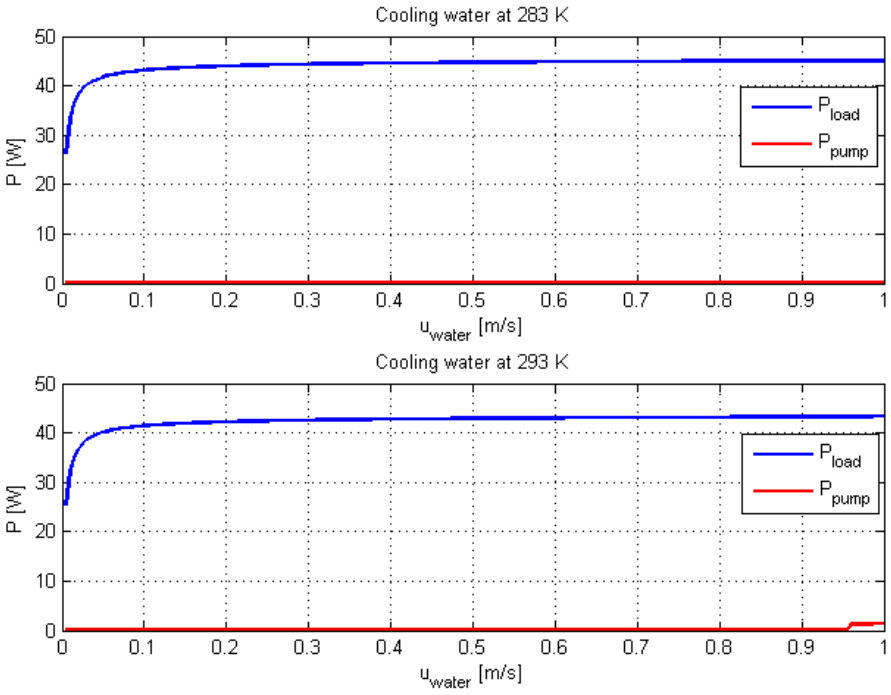

Figure 6.5: Water cooled WHRS power production as a function of the water velocity.

6.2 Air cooled WHRS results

The working conditions assumed in the previous section were carried out for the optimal air cooled WHRS, therefore the simulations are not described and the results

are directly presented and discussed.

6.2.1 Simulation 1. Performance for variable exhaust gas mass flow

As seen in Figure 6.6, the power consumption of the compressor used to circulate the cooling air is much higher than the consumption of the pump used to circulate the cooling water. Since the water is a better coolant than the air, the flow regime of the air has to be turbulent. In addition, power is provided to the load at the minimum exhaust gas mass flow rate, however the WHRS does not has a positive net power production until a mass flow higher than 10 g/s flows through the HSHX. The minimum, mean and maximum power provided to the load are 2.95, 31.94 and 54.58 W.

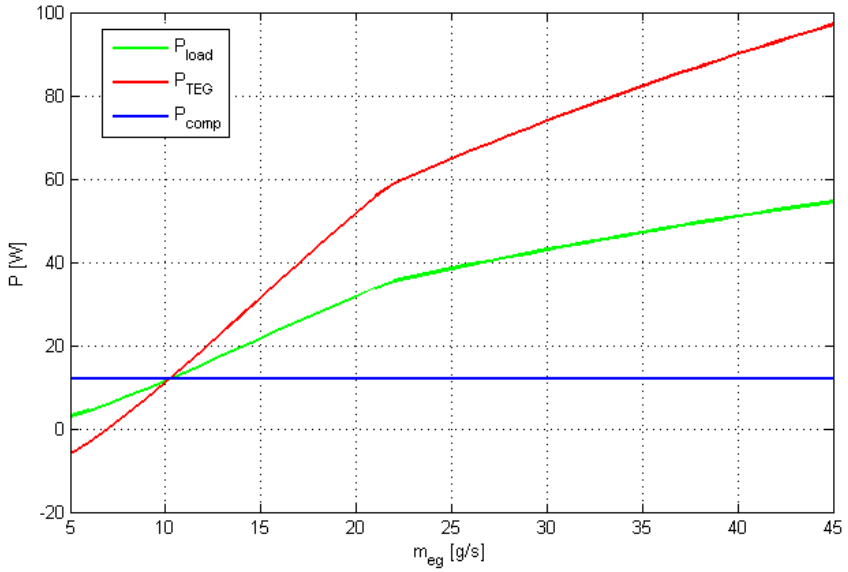

Figure 6.6: Air cooled WHRS power production as a function of the exhaust gas mass flow.

The voltage and current curves as a function of the exhaust gas mass flow rate can be seen in Figure 6.7. The minimum, mean and maximum load voltage values are 0.78, 2.56 and 3.45 V, while the current values are 3.79, 12.45 and 16.77 A. The production is lower than in the water cooled WHRS, although the air cooled WHRS has more thermoelectric pellets.

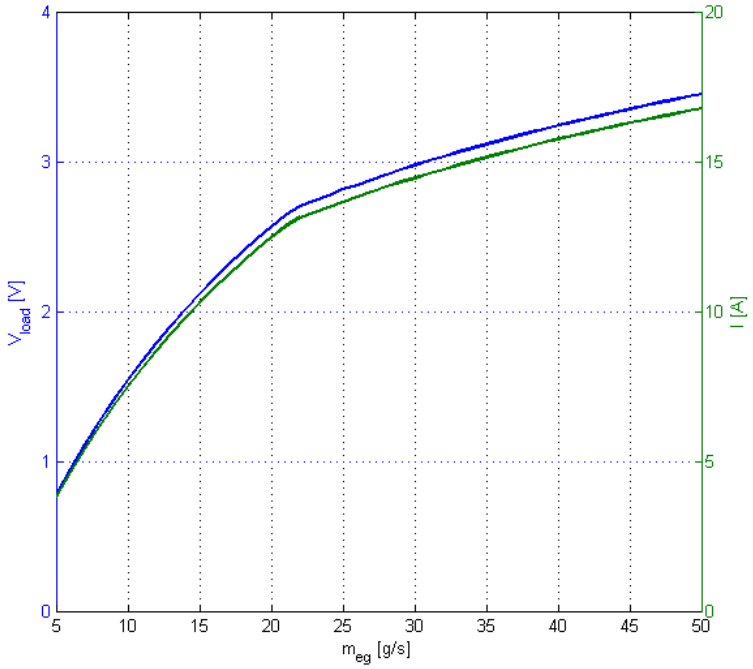

Figure 6.7: Air cooled WHRS voltage and current production as a function of the exhaust gas mass flow.

6.2.2 Simulation 2. Performance for variable electric load

The power production of the WHRS can be seen in Figure 6.8. Due to the high power consumption of the WHRS cooling system, the value of the load that can be supplied is limited, since the system was optimized for matched electric impedance condition. For loads higher than 1.8 Ω, the power provided to the load does not compensate the cooling power consumption. Therefore the optimized air cooled WHRS can not be used for high load values.

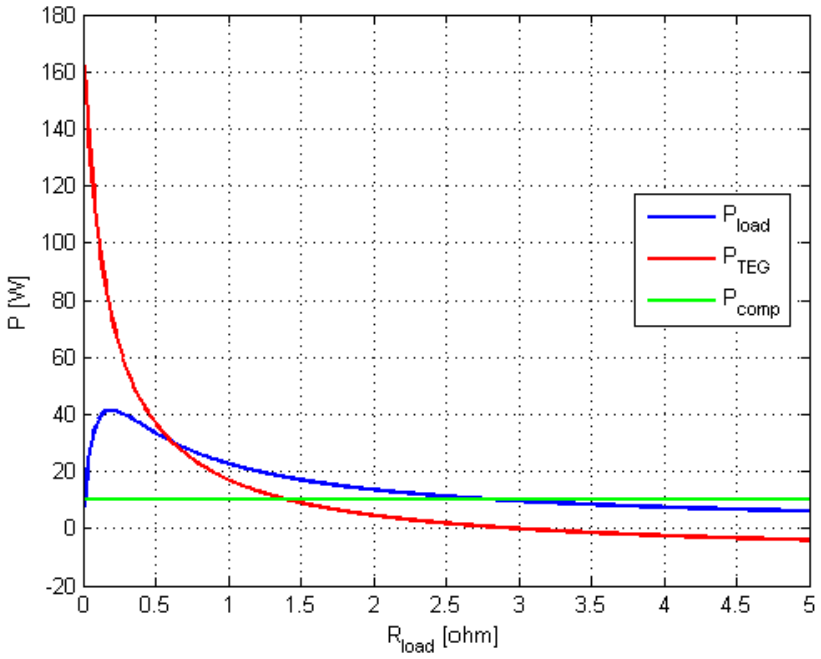

Figure 6.8: Water cooled WHRS power production as a function of the electric load value.

6.2.3 Simulation 3. Performance for variable cooling air velocity

The power provided to the load and the cooling air compressor power consumption are shown in Figure 6.9 as a function of the cooling air velocity. The optimal cooling air velocity provided by the optimization procedure is 14.83 m/s, however in the figure it is observed that the maximum net power production takes place at 6 m/s. On the other hand, it can be seen that velocity values higher than 15 m/s provide a much lower net power production. This implies that the bounds within the air cooled WHRS optimization problem were too strict, relaxing this bounds, could have require lower velocities to ensure the thermal impedance match condition.

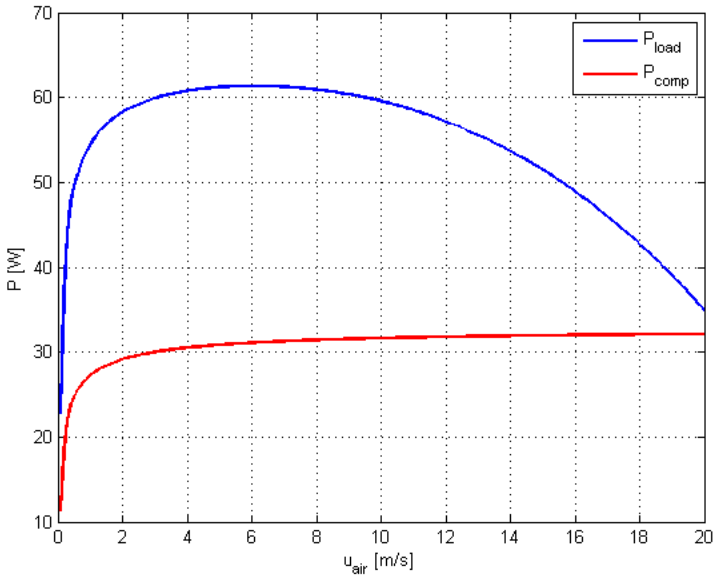

Figure 6.9: Air cooled WHRS power production as a function of the air velocity.

Chapter 7

Conclusion

In this project, the feasibility of implementing a TEG based WHRS for an automobile engine has been determined. As seen in this report, the TEG implementation requires a heat exchanger network to transfer the heat from the engine exhaust gas to the generator, and a heat sink to obtain an adequate temperature gradient across it. The possibility of using air and water as heat sink coolant was considered.

The WHRS was optimized based on an analytical model. The analytical model was tried to be validate by means of an experimental setup and a CFD simulation.

The CFD simulation was found to be not conclusive and therefore did not allow to validate the analytical model. A CFD simulation is really time consuming and computationally demanding. Although the used CFD software has a friendly user interface, a proper knowledge of the software is required to obtain conclusive results. Therefore the validation of the model was reduced to the experimental work.

The heat exchanger network was probed to be valid through the experimental work, however the TEG thermal model was found not valid. Because of the limitation of the designed experimental setup, the TEG module could just be tested for low temperature gradients. A smaller size TEG module and HSHX cross section area should have been used in order to test the module at higher temperatures. Experimental work at higher temperatures may lead to a different conclusion.

In spite of the model veracity, the optimization procedure was carried out and an optimal design was obtained based on the analytical model. Real car engine working conditions and materials were used as boundary conditions of the optimization problem. An insight into the requirements the optimal design has to meet was obtained. This is high exhaust gas velocity values in the hot side heat exchanger and either large heat exchange surface between the cooling fluid and the heat sink or high cooling fluid velocities.

The performance of both water and air cooled WHRS was predicted based on the analytical model, being aware of its limitation within the TEG module performance. A more accurate TEG model should be obtained in order to predict reliable power production values. However it provides an insight of the WHRS performance.

It was proved that both systems can be implemented and produce usable voltage

and current values. However the simulated air cooled WHRS design was found not to be the optimal solution. Therefore it can not be concluded which system is better. Comparing the simulations results, the water cooled WHRS shows a higher net power production, since the consumption of the cooling utilities is lower than in the air case. The restrictions imposed to the HS geometry in the optimization problem, made the fluid velocity adopt high velocities. Higher fluid velocities imply higher pumping demand and thus higher power consumption. Therefore the net power of the air cooled WHRS was found to have lower net power production, compared to the water cooled WHRS.

A design reduced in size is most likely to be desired in order to integrate the TEG based WHRS in a car, this implies that the water cooled WHRS is a better candidate.

7.1 Future work

The CFD simulation was a promising task but lead us to a dead-end and the possibilities that such a software has was not exploited. Apart from the features used in this project, ANSYS includes a Thermal-Electric analysis system. The simultaneous use of FLUENT and Thermal-Electric would lead to really accurate predictions. Therefore future work should be done within this tool.

The possibility of using a rectangular duct as heat exchanger was solely considered. More complex designs have to be examined in order to improve the WHRS design. In addition, covering more heat exchanger outer surface with thermoelectric material should be considered to increase the waste heat recovery.

Bibliography

Agilent (2012). Agilent 34970A Data Acquisition / Switch Unit The Front Panel at a Glance.

ANSYS®, A. R. (2014a). Help system , FLUENT mesh quality.

ANSYS®, A. R. (2014b). Help system: Theory guide.

Baranowski, L. L., Jeffrey Snyder, G., and Toberer, E. S. (2013). Effective thermal conductivity in thermoelectric materials. *Journal of Applied Physics*, 113.

Bitschi, A. (2009). Modelling of Thermoelectric Devices for Electric Power Generation. (18441).

Casey, M. and Wintergerste, T. (2000). *ERCOFTAC - Best Practice Guidelines*.

Çengel, Y. A. (2003). *Heat transfer: A practical approach*. McGraw Hill.

Ceramics, C. T. (2015). AD-96 Alumina: Aluminum Oxide.

Crowe, C. T. (2010). Engineering Fluid Mechanics.

General Motors (2011). Benefits of Thermoelectric Technology for the Automobile. pages 1–15.

Gnielinski, V. (2010). VDI Heat Atlas. chapter G1 Heat Tr, pages 691–700. Springer Berlin Heidelberg, Berlin, Heidelberg.

Honsberg, C. and Bowden, S. (2014). http://pveducation.org/.

Http://swema.com/ (2015). Swema webpage.

Lund, E. (2015). AAU Optimization Course - Lecture Slides.

Mendes, F. (2011). Non-linear equations system solver (Newton Raphson).

Min, G. (2005). Thermoelectric Module Design Theories. In *Thermoelectrics Handbook*, pages 11–15. CRC Press.

Ohio.University (2015). Lecture 13 Nonlinear Systems - Newton ' s Method. pages 46–49.

Rezania, a. and Rosendahl, L. a. (2012). Thermal effect of ceramic substrate on heat distribution in thermoelectric generators. *Journal of Electronic Materials*, 41(6):1343–1347.

Rezania, a., Yazawa, K., Rosendahl, L. a., and Shakouri, a. (2013). Co-optimized design of microchannel heat exchangers and thermoelectric generators. *International Journal of Thermal Sciences*, 72:73–81.

Rotron, C. (2015). Brushless DC Fans.

Rowe, D. M. (2005). General Principles and Basic Considerations. In *Thermoelectrics Handbook*, chapter Chapter 1, pages 1–14. CRC Press.

Sparrow, E. M., Abraham, J. P., and Minkowycz, W. J. (2009). Flow separation in a diverging conical duct: Effect of Reynolds number and divergence angle. *International Journal of Heat and Mass Transfer*, 52(13-14):3079–3083.

Stevens, R. J., Weinstein, S. J., and Koppula, K. S. (2014). Theoretical limits of thermoelectric power generation from exhaust gases. *Applied Energy*, 133:80–88.

Tellurex (2006). The Most Frequently Asked Questions About Thermoelectric Power Generation Technology. *Technology*.

Tuckerman, D. and Pease, R. (1981). High-performance heat sinking for VLSI. *IEEE Electron Device Letters*, 2(5):126–129.

Veersteeg, H.K , Malalasekera, W. (2007). *An introduction to computational fluid dynamics – The finite volume method*. Pearson Education Limited, 2nd editio edition.

Wang, Y., Dai, C., and Wang, S. (2013). Theoretical analysis of a thermoelectric generator using exhaust gas of vehicles as heat source. *Applied Energy*, 112:1171–1180.

Appendix A: DC fan volumetric flow determination

The volumetric flow provided by the DC fan was determined as a function of its DC voltage. To achieve it, the setup in Figure .0.1 was developed. It consists on a 60 mm diameter pipe with a length of 500 mm with converging inlet to minimize the pressure loss of the inlet. A small hole was made in the duct. The velocity of the air was measured with an air velocity meter Swema 3000, shown in Figure .0.2. Its probe was placed in the middle of the duct. It was decided to fix the probe handle to the workbench in order to avoid variations in the probe position. The device measures the velocity of the air and known the section, the volumetric flow can be determined. In addition, the temperature of the air inside the duct was measured with the device. The fan was powered by a DC power supply (TTI CPX 400SP). The voltage was varied from 4 up to 15.5 volts. The current at this voltage value was 1.24 amp, thus the experiment was stopped since the maximum current according to the manufacturer is 1.4. The voltage was increased by 0.5 volts steps. The velocity of the air was measured at every voltage value. The results are plotted in Figure .0.3.

Figure .0.1: DC fan flow measurement setup.

Figure .0.2: Used air velocity meter [Http://swema.com/, 2015].

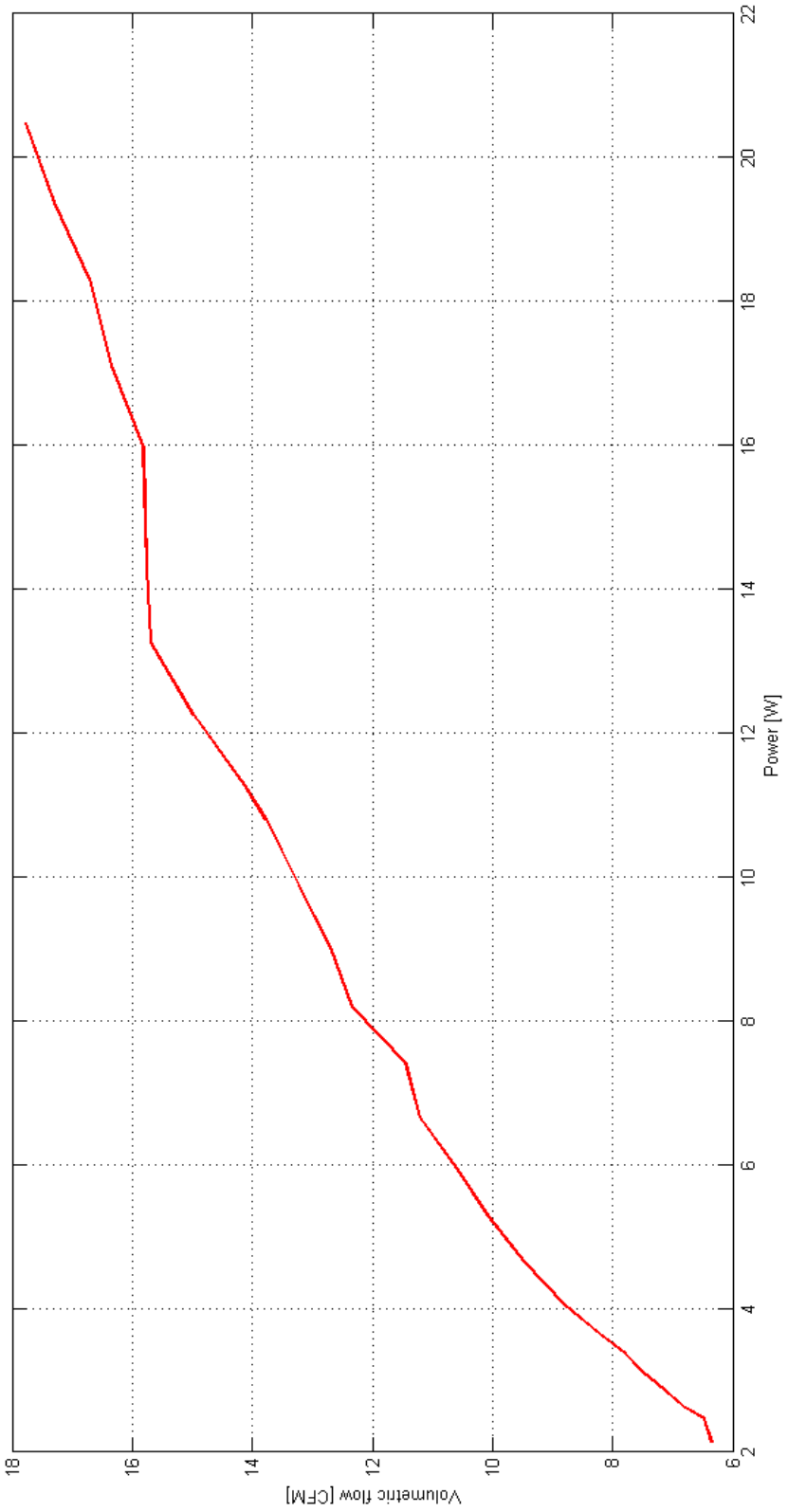

Figure .0.3: DC fan test results.

Appendix B: CFD turbulence models coefficients calculation

In this appendix the calculation of the coefficients used to solve Equation 4.9 and 4.10 for the kinetic (k) and its dissipation rate (ω) in k-ω turbulent model. In these equations, G_k represents the generation of turbulence kinetic energy due to mean velocity gradients. G_ω represents the generation of ω . Γ_k and Γ_ω represent the effective diffusivity of k and ω , respectively. Y_k and Y_ω represent the dissipation of k and ω due to turbulence.

The effective diffusivities in the k-ω model are given by Equation 1 and Equation 2.

$$\Gamma_k = \mu + \frac{\mu_t}{\Phi_k} \tag{1}$$

$$\Gamma_\omega = \mu + \frac{\mu_t}{\Phi_\omega} \tag{2}$$

The turbulent viscosity (μ_t) is computed by Equation 3

$$\mu_t = a^* \frac{\rho k}{\omega} \tag{3}$$

a^* coefficient damps the turbulent viscosity given by equation 4

$$a^* = a^*_\infty \left(\frac{a^*_0 + Re_t/R_k}{1 + Re_t/R_k}\right) \tag{4}$$

where

$$Re_t = \frac{\rho k}{\mu \omega} \tag{5}$$

$$Re_k = 6 \tag{6}$$

$$\alpha_0^* = \frac{\beta_i}{3} \tag{7}$$

$$\beta_i = 0.072 \tag{8}$$

G_k is the generation of turbulence kinetic energy , calculated using equation 9

$$G_k = -\rho\overline{u_i' u_j'}\frac{\partial u_j}{\partial x_j} \tag{9}$$

G_ω is the generation of ω

$$G_\omega = a\frac{\omega}{k}G_k \tag{10}$$

where G_k is given by equation 9 and a^*

$$a^* = \frac{a_\infty}{a^*}(\frac{a_0 + Re_t/R_\omega}{1 + Re_t/R_\omega}) \tag{11}$$

where $R_\omega = 2.95$. a and Re_t are given by equations 4-5.
The dissipation of k is given by equation 12

$$Y_k = \rho\beta^* f_{\beta^*} k\omega \tag{12}$$

where

$$f_{\beta^*} = \begin{cases} 1 & \varsigma_k \leq 0 \\ \frac{1+680\varsigma_k^2}{1+400\varsigma_k^2} & \varsigma_k > 0 \end{cases}$$

where

$$\varsigma = \frac{1}{\omega^3}\frac{\partial k}{\partial x_j}\frac{\partial \omega}{\partial x_j} \tag{13}$$

and

$$\beta^* = \beta_i^*[1 + \zeta^* F(M_t)] \tag{14}$$

$$\beta_i^* = \beta_\infty^*(\frac{4/15 + (Re - t/Re - \beta)^4}{1 + (Re - t/Re - \beta)^4}) \tag{15}$$

$$\zeta^* = 1.5 \tag{16}$$

$$R^\beta = 8 \tag{17}$$

$$\beta_\infty^* = 0.09 \tag{18}$$

Dissipation of ω is given by equation 19

$$Y_\omega = \rho\beta f_\beta \omega^2 \tag{19}$$

where

$$f_{beta} = \frac{1 + 70\varsigma_\omega}{1 + 80\varsigma_\omega} \tag{20}$$

$$\varsigma_\omega = |\frac{\Upsilon_{ij}\Upsilon_{ik}S - ki}{(\beta_\infty^*\omega)^3}| \tag{21}$$

$$\Upsilon_{ij} = \frac{1}{2}(\frac{\partial u_i}{\partial x_j} - \frac{\partial u_j}{\partial x_i}) \tag{22}$$

Appendix C: Newton's method

The set of equations described in Chapter 2 includes non-linear equations. In the CD attached to this report, the MATLAB code used to solve the set of equations can be found. The algorithm is based on Newton's method [Mendes, 2011]. In this appendix a short description of the method is made.

The idea behind this method is finding iteratively the values for x_1 to x_n, that makes a given set of n equations equal to zero.

First a set of initial values are guessed, in the code they are generated aleatory. A counter for the number of iterations is set to zero. A maximum number of iterations is set and a tolerance ϵ are set as stop criteria. The algorithm computes iteratively a new point based on the previous point according to Equation 1 and Equation 2 [Ohio.University, 2015].

$$x_{k+1} = x_k + \Delta x \tag{1}$$

$$\Delta x = -f(x_k) \cdot Df(x_k)^{-1} \tag{2}$$

Where $f(x_k)$ is a vector that includes the values of each equation at the point x_k and $Df(x_k)$ is a $n \times n$ matrix that includes the partial derivatives of the different unknowns.

The counter is updated and the new calculated point is used to compute the following point. The calculation is repeated till Δx is smaller than ϵ or the maximum number of iterations is reached.